4-1-2021

# A Search for Correlations between Turbulence and Star Formation in LITTLE THINGS Dwarf Irregular Galaxies

Deidre A. Hunter
*Lowell Observatory*

Bruce G. Elmegreen
*IBM Thomas J. Watson Research Center*

Haylee Archer
*Lowell Observatory*

Caroline E. Simpson
*Florida International University*

Phil Cigan
*George Mason University*

# A Search for Correlations between Turbulence and Star Formation in LITTLE THINGS Dwarf Irregular Galaxies

Deidre A. Hunter[1] , Bruce G. Elmegreen[2] , Haylee Archer[1], Caroline E. Simpson[3] , and Phil Cigan[4]
[1] Lowell Observatory, 1400 West Mars Hill Road, Flagstaff, AZ 86001, USA
[2] IBM T.J. Watson Research Center, 1101 Kitchawan Road, Yorktown Heights, NY USA
[3] Department of Physics, Florida International University, CP 204, 11200 SW 8th Street, Miami, FL 33199 USA
[4] George Mason University, 4400 University Drive, Fairfax, VA 22030-4444, USA

## Abstract

Turbulence has the potential for creating gas density enhancements that initiate cloud and star formation (SF), and it can be generated locally by SF. To study the connection between turbulence and SF, we looked for relationships between SF traced by FUV images, and gas turbulence traced by kinetic energy density (KED) and velocity dispersion ($v_{\mathrm{disp}}$) in the LITTLE THINGS sample of nearby dIrr galaxies. We performed 2D cross-correlations between FUV and KED images, measured cross-correlations in annuli to produce correlation coefficients as a function of radius, and determined the cumulative distribution function of the cross-correlation value. We also plotted on a pixel-by-pixel basis the locally excess KED, $v_{\mathrm{disp}}$, and H I mass surface density, $\Sigma_{\mathrm{HI}}$, as determined from the respective values with the radial profiles subtracted, versus the excess SF rate density $\Sigma_{\mathrm{SFR}}$, for all regions with positive excess $\Sigma_{\mathrm{SFR}}$. We found that $\Sigma_{\mathrm{SFR}}$ and KED are poorly correlated. The excess KED associated with SF implies a $\sim$0.5% efficiency for supernova energy to pump local H I turbulence on the scale of the resolution here, which is a factor of $\sim$2 too small for all of the turbulence on a galactic scale. The excess $v_{\mathrm{disp}}$ in SF regions is also small, only $\sim$0.37 km s$^{-1}$. The local excess in $\Sigma_{\mathrm{HI}}$ corresponding to an excess in $\Sigma_{\mathrm{SFR}}$ is consistent with a H I consumption time of $\sim$1.6 Gyr in the inner parts of the galaxies. The similarity between this timescale and the consumption time for CO implies that CO-dark molecular gas has comparable mass to H I in the inner disks.

*Unified Astronomy Thesaurus concepts:* Dwarf irregular galaxies (417)

*Supporting material:* extended figures

## 1. Introduction

The gas in the inner parts of spiral galaxies is gravitationally unstable to the formation of clouds that can go on to form stars (Toomre 1964; Kennicutt 1989). However, in dwarf irregular (dIrr) galaxies, the atomic gas densities are much lower than in spirals and are apparently stable against this instability (Hunter & Plummer 1996; Meurer et al. 1996; van Zee et al. 1997; Hunter et al. 2011). Furthermore, in inner spiral disks, star formation increases as the gas density increases (Bigiel et al. 2008), while in dwarfs and outer spiral disks, the atomic gas density cannot predict star formation rates (SFRs; Bigiel et al. 2010). So, what drives star formation in dIrr galaxies?

One process for creating clouds is the compression of gas in a supersonically turbulent medium (Elmegreen 1993; Mac Low & Klessen 2004). There is extensive evidence for interstellar turbulence in galaxies, and turbulence in typical dIrrs has been shown to be transonic (Burkhart et al. 2010; Maier et al. 2017) while that in spirals is generally supersonic (Maier et al. 2016). Furthermore, various distributions in the stellar, cluster, and cloud properties in dwarfs are consistent with sampling a fractal turbulent gas, including composite cumulative H II region luminosity functions (Youngblood & Hunter 1999; Kingsburgh & McCall 1998), stellar disk power spectra (Willett et al. 2005), mass functions of clouds and star clusters (Elmegreen & Efremov 1997; Hunter et al. 2003; Mac Low & Klessen 2004), Hα probability distribution functions (Hunter & Elmegreen 2004), and the correlation between region size and the star formation timescale (Efremov & Elmegreen 1998). Dib & Burkert (2005) found evidence for scales in the interstellar medium (ISM) of Holmberg II less than 6 kpc in size that they interpret to be due to

a turbulence driver acting on that scale. Zhang et al. (2012) showed from H I spatial power spectra that either nonstellar power sources are playing a fundamental role in driving the ISM turbulence or the nonlinear development of turbulent structures has little to do with the driving sources. In addition, Hunter et al. (2001, 2011) have found regions of high-velocity dispersion in the H I distribution of some dIrr galaxies that correlate with a deficit of H I in a manner suggestive of long-range, turbulent pressure equilibrium (Piontek & Ostriker 2005).

Turbulence can create density enhancements that initiate cloud formation (Krumholz & McKee 2005), but turbulence also heats gas, which can make it harder to form clouds (Struck & Smith 1999). So, how important is turbulence in driving star formation in dwarfs? It could be essential in outer disks where gas self-gravity is weak (Elmegreen & Hunter 2006). Also, a transition from subsonic to supersonic turbulence in the ISM could be the cause of the transition in the Schmidt–Kennicutt SFR–gas density relationship from inefficient star formation at low gas surface densities to star formation at higher densities (Kraljic et al. 2014).

Conversely, how important is star formation in driving turbulence? Simulations suggest that stellar feedback and supernovae drive turbulence on the scale of the galaxy thickness (Joung et al. 2009; Kim & Ostriker 2015), and it may drive turbulence in molecular clouds (Padoan et al. 2016), along with cloud self-gravity (Ibáñez-Mejía et al. 2017; Mac Low et al. 2017). Feedback destroys molecular clouds as well (Kim et al. 2018; Chevance et al. 2020). Models also suggest feedback controls the SFR by adjusting the disk thickness and midplane density (Ostriker et al. 2010) or by compressing nearby clouds, causing them to collapse (Deharveng et al. 2012; Egorov et al. 2017;

Palmeirim et al. 2017). On a galactic scale, feedback and self-gravity operate together to drive turbulence (e.g., Goldbaum et al. 2016; Krumholz et al. 2018). These models are uncertain, however. Other simulations show no need for star formation to drive turbulence because they reproduce the velocity dispersion from self-gravity alone; the only thing local feedback needs to do is destroy the clouds where young stars form, preventing the SFR from getting too large (Bournaud et al. 2010; Combes et al. 2012; Hopkins et al. 2011).

Observations are usually not decisive about the connection between the SFR and turbulence. In a study of local dwarfs and low-mass spirals, Stilp et al. (2013) found a correlation between the core velocity dispersion in H I line profiles and the H I surface density, suggestive of driving by gravitational instabilities, but they also found a correlation with SFR at $\Sigma_{SFR} > 10^{-4} \, M_\odot \, \mathrm{yr}^{-1} \, \mathrm{kpc}^{-2}$. Stilp et al. (2013) show that both the H I velocity dispersion and $\Sigma_{SFR}$ decrease with radius in a galaxy; that makes correlations between these quantities ambiguous as they both could depend on another parameter that varies with radius and not each other.

Zhou et al. (2017) studied eight local galaxies with resolved spectroscopy and showed on a pixel level that the velocity dispersion of ionized gas does not change over a factor of ∼40 in SFR per unit area. Also, for several hundred local galaxies in the same survey, Varidel et al. (2020) found a very small correlation between the galaxy-average vertical velocity dispersion of ionized gas and the total SFR, with the dispersion increasing by only 6 km s⁻¹ for SFRs between $10^{-3}$ and 10 $M_\odot$ yr⁻¹. This contrasts with observations of high-redshift galaxies where these authors show strong increases in dispersion with SFR density and total rate, respectively, for rate densities larger than ∼0.1 $M_\odot$ yr⁻¹ kpc⁻² and rates higher than ∼3 $M_\odot$ yr⁻¹. This high-redshift correlation was earlier studied by several groups, including Lehnert et al. (2013), who observed that the velocity dispersion of ionized gas increases as the square root of the SFR per unit area. Lehnert et al. (2013) concluded that star formation was the main driver of turbulence and that it was also sufficient to maintain marginal stability in a disk. On the other hand, Übler et al. (2019) interpreted the increase in the ionized gas velocity dispersion with SFR density for high-redshift galaxies as the result of gravitational instabilities, following the theory in Krumholz et al. (2018).

Bacchini et al. (2020) consider radial profiles of turbulent speeds and SFRs in local spiral galaxies and account for all of the gas turbulence using supernovae from young massive stars. They get more effective turbulence driving than other studies because they include the radial increase in disk thickness, which decreases the dissipation rate.

In this paper, we look for evidence of a spatial correlation between star formation and turbulence in the LITTLE THINGS sample of nearby dIrr galaxies. A spatial correlation could be either a cause of star formation through the production of a gas cloud or a result of star formation through mechanical energy input to the local ISM through feedback from stars. We construct turbulent kinetic energy density (KED) maps from the kinetic energy associated with the bulk motions of the gas —velocity from H I velocity dispersion (moment 2) and mass from integrated column density (moment 0) maps, per unit area in the galaxy. We cross-correlate the KED maps with far-ultraviolet (FUV) images that trace star formation over the past 200 Myr. Because we are using intensity-weighted velocity dispersions, the "turbulence" includes all bulk motions of the

gas, including thermal and turbulent. This follows the two-dimensional (2D) cross-correlation method used by I. Bagetakos (2018, private communication) in the analysis of the spiral galaxy NGC 2403.

We also isolate turbulence in the vicinity of a star formation region and determine the excess KED and velocity dispersion from that region alone. This method removes any background turbulence that may be generated by other means, such as gravitational instabilities and collapse.

## 2. Data

LITTLE THINGS[5] is a multiwavelength survey of nearby dwarf galaxies (Hunter et al. 2012). The LITTLE THINGS sample comprises 37 dIrr galaxies and 4 Blue Compact Dwarf (BCD) galaxies. The galaxies are relatively nearby (⩽10.3 Mpc; 6″ is ⩽300 pc), contain gas so they have the potential for star formation, and are not companions to larger galaxies. The sample also covers a large range in dwarf galactic properties such as SFR and absolute magnitude.

We obtained H I observations of the LITTLE THINGS galaxies with the National Science Foundation's Karl G. Jansky Very Large Array (VLA[6]). The H I-line data are characterized by high sensitivity (⩽1.1 mJy beam⁻¹ per channel), high spectral resolution (1.3 or 2.6 km s⁻¹), and high angular resolution (typically 6″).

Ancillary data used here include far-ultraviolet (FUV) images obtained with the NASA Galaxy Evolution Explorer satellite (GALEX[7]; Martin et al. 2005). These images trace star formation over the past 200 Myr. These data also yield integrated SFRs (Hunter et al. 2010) and the radius at which we found the farthest-out FUV knot $R_{FUV \, knot}$ in each galaxy (Hunter et al. 2016). The SFRs are normalized to the area within one disk scale length $R_D$, although star formation is usually found beyond $1R_D$. $R_D$ is measured from V-band surface brightness profiles (Herrmann et al. 2013). Several of the LITTLE THINGS galaxies without GALEX FUV images are not included in this study (DDO 155, DDO 165, IC 10, UGC 8508). Pixel values of FUV and $\Sigma_{SFR}$ are not corrected for extinction due to dust, which tends to be low in these low-metallicity galaxies.

The galaxy sample and characteristics that we use here are given in Table 1. In some plots, we distinguish between those dIrrs that are classified as Magellanic irregulars (dIm) and those that are classified as BCDs (Haro 29, Haro 36, Mrk 178, VIIZw403).

## 3. Cross-correlations

### 3.1. Two-dimensional

KED and FUV images were the inputs to the 2D cross-correlation. We geometrically transformed the FUV image to match the orientation and field of view (FOV) of the H I map using OHGEO in the Astronomical Image Processing System

**Table 1**
The Galaxy Sample

| Galaxy | $D^a$ (Mpc) | $M_V$ | $R_{H\alpha}^b$ (kpc) | $R_{FUV\ knot}^c$ (kpc) | $R_D^d$ (kpc) | $R_{Br}^e$ (kpc) | logSFR$_D^{FUV f}$ ($M_\odot$ yr$^{-1}$ kpc$^{-2}$) |
|---|---|---|---|---|---|---|---|
| CVnIdwA | 3.6 ± 0.08 | −12.37 ± 0.09 | 0.69 | 0.49 ± 0.03 | 0.25 ± 0.12 | 0.56 ± 0.49 | −1.77 ± 0.04 |
| DDO 43 | 7.8 ± 0.8 | −15.06 ± 0.22 | 2.36 | 1.93 ± 0.08 | 0.87 ± 0.10 | 1.46 ± 0.53 | −2.20 ± 0.04 |
| DDO 46 | 6.1 ± 0.4 | −14.67 ± 0.16 | 1.51 | 3.02 ± 0.06 | 1.13 ± 0.05 | 1.27 ± 0.18 | −2.45 ± 0.04 |
| DDO 47 | 5.2 ± 0.6 | −15.46 ± 0.24 | 5.58 | 5.58 ± 0.05 | 1.34 ± 0.05 | ⋯ | −2.38 ± 0.04 |
| DDO 50 | 3.4 ± 0.05 | −16.61 ± 0.03 | ⋯ | 4.86 ± 0.03 | 1.48 ± 0.06 | 2.65 ± 0.27 | −1.81 ± 0.04 |
| DDO 52 | 10.3 ± 0.8 | −15.45 ± 0.17 | 3.69 | 3.39 ± 0.10 | 1.26 ± 0.04 | 2.80 ± 1.35 | −2.53 ± 0.04 |
| DDO 53 | 3.6 ± 0.05 | −13.84 ± 0.03 | 1.25 | 1.19 ± 0.03 | 0.47 ± 0.01 | 0.62 ± 0.09 | −1.96 ± 0.04 |
| DDO 63 | 3.9 ± 0.05 | −14.78 ± 0.03 | 2.26 | 2.89 ± 0.04 | 0.68 ± 0.01 | 1.31 ± 0.10 | −2.05 ± 0.04 |
| DDO 69 | 0.8 ± 0.04 | −11.67 ± 0.11 | 0.76 | 0.76 ± 0.01 | 0.19 ± 0.01 | 0.27 ± 0.05 | −2.22 ± 0.04 |
| DDO 70 | 1.3 ± 0.07 | −14.10 ± 0.12 | 1.23 | 1.34 ± 0.01 | 0.44 ± 0.01 | 0.13 ± 0.07 | −2.17 ± 0.04 |
| DDO 75 | 1.3 ± 0.05 | −13.91 ± 0.08 | 1.17 | 1.38 ± 0.01 | 0.18 ± 0.01 | 0.71 ± 0.08 | −0.99 ± 0.04 |
| DDO 87 | 7.7 ± 0.5 | −14.98 ± 0.15 | 3.18 | 4.23 ± 0.07 | 1.21 ± 0.02 | 0.99 ± 0.11 | −2.61 ± 0.04 |
| DDO 101 | 6.4 ± 0.5 | −15.01 ± 0.16 | 1.23 | 1.23 ± 0.06 | 0.97 ± 0.06 | 1.16 ± 0.11 | −2.84 ± 0.04 |
| DDO 126 | 4.9 ± 0.5 | −14.85 ± 0.24 | 2.84 | 3.37 ± 0.05 | 0.84 ± 0.13 | 0.60 ± 0.05 | −2.18 ± 0.04 |
| DDO 133 | 3.5 ± 0.2 | −14.75 ± 0.16 | 2.60 | 2.20 ± 0.03 | 1.22 ± 0.04 | 2.25 ± 0.24 | −2.60 ± 0.04 |
| DDO 154 | 3.7 ± 0.3 | −14.19 ± 0.16 | 1.73 | 2.65 ± 0.04 | 0.48 ± 0.02 | 0.62 ± 0.09 | −1.77 ± 0.04 |
| DDO 167 | 4.2 ± 0.5 | −12.98 ± 0.25 | 0.81 | 0.70 ± 0.04 | 0.22 ± 0.01 | 0.56 ± 0.11 | −1.59 ± 0.04 |
| DDO 168 | 4.3 ± 0.5 | −15.72 ± 0.25 | 2.24 | 2.25 ± 0.04 | 0.83 ± 0.01 | 0.72 ± 0.07 | −2.06 ± 0.04 |
| DDO 187 | 2.2 ± 0.07 | −12.68 ± 0.07 | 0.30 | 0.42 ± 0.02 | 0.37 ± 0.06 | 0.28 ± 0.05 | −2.60 ± 0.04 |
| DDO 210 | 0.9 ± 0.04 | −10.88 ± 0.10 | ⋯ | 0.29 ± 0.01 | 0.16 ± 0.01 | ⋯ | −2.66 ± 0.04 |
| DDO 216 | 1.1 ± 0.05 | −13.72 ± 0.10 | 0.42 | 0.59 ± 0.01 | 0.52 ± 0.01 | 1.77 ± 0.45 | −3.17 ± 0.04 |
| F564-V3 | 8.7 ± 0.7 | −13.97 ± 0.18 | ⋯ | 1.24 ± 0.08 | 0.63 ± 0.09 | 0.73 ± 0.40 | −2.94 ± 0.04 |
| IC 1613 | 0.7 ± 0.05 | −14.60 ± 0.16 | ⋯ | 1.77 ± 0.01 | 0.53 ± 0.02 | 0.71 ± 0.12 | −1.97 ± 0.04 |
| LGS 3 | 0.7 ± 0.08 | −9.74 ± 0.25 | ⋯ | 0.32 ± 0.01 | 0.16 ± 0.01 | 0.27 ± 0.08 | −3.75 ± 0.04 |
| M81dwA | 3.6 ± 0.2 | −11.73 ± 0.13 | ⋯ | 0.71 ± 0.03 | 0.27 ± 0.00 | 0.38 ± 0.03 | −2.30 ± 0.04 |
| NGC 1569 | 3.4 ± 0.2 | −18.24 ± 0.13 | ⋯ | 1.14 ± 0.03 | 0.46 ± 0.02 | 0.85 ± 0.24 | −0.32 ± 0.04 |
| NGC 2366 | 3.4 ± 0.3 | −16.79 ± 0.20 | 5.58 | 6.79 ± 0.03 | 1.91 ± 0.25 | 2.57 ± 0.80 | −2.04 ± 0.04 |
| NGC 3738 | 4.9 ± 0.5 | −17.12 ± 0.24 | 1.48 | 1.21 ± 0.05 | 0.77 ± 0.01 | 1.16 ± 0.20 | −1.52 ± 0.04 |
| NGC 4163 | 2.9 ± 0.04 | −14.45 ± 0.03 | 0.88 | 0.47 ± 0.03 | 0.32 ± 0.00 | 0.71 ± 0.48 | −1.89 ± 0.04 |
| NGC 4214 | 3.0 ± 0.05 | −17.63 ± 0.04 | ⋯ | 5.46 ± 0.03 | 0.75 ± 0.01 | 0.83 ± 0.14 | −1.11 ± 0.04 |
| Sag DIG | 1.1 ± 0.07 | −12.46 ± 0.14 | 0.51 | 0.65 ± 0.01 | 0.32 ± 0.05 | 0.57 ± 0.14 | −2.40 ± 0.04 |
| WLM | 1.0 ± 0.07 | −14.39 ± 0.15 | 1.24 | 2.06 ± 0.01 | 1.18 ± 0.24 | 0.83 ± 0.16 | −2.78 ± 0.04 |
| Haro 29 | 5.8 ± 0.3 | −14.62 ± 0.11 | 0.96 | 0.86 ± 0.06 | 0.33 ± 0.00 | 1.15 ± 0.26 | −1.21 ± 0.04 |
| Haro 36 | 9.3 ± 0.6 | −15.91 ± 0.15 | 1.06 | 1.79 ± 0.09 | 1.01 ± 0.00 | 1.16 ± 0.13 | −1.88 ± 0.04 |
| Mrk 178 | 3.9 ± 0.5 | −14.12 ± 0.26 | 1.17 | 1.45 ± 0.04 | 0.19 ± 0.00 | 0.38 ± 0.00 | −1.17 ± 0.04 |
| VIIZw403 | 4.4 ± 0.07 | −14.27 ± 0.04 | 1.27 | 0.33 ± 0.04 | 0.53 ± 0.02 | 1.02 ± 0.29 | −1.80 ± 0.04 |

**Notes.**
[a] Distance to the galaxy. References are given by Hunter et al. (2012).
[b] Radius of farthest-out detected H II region $R_{H\alpha}$ in each galaxy from Hunter & Elmegreen (2004). Galaxies without H II regions or with H II regions extending beyond the area imaged do not have $R_{H\alpha}$.
[c] Radius of farthest-out detected FUV knot $R_{FUV\ knot}$ in each galaxy from Hunter et al. (2016). Galaxies without GALEX images have no value for this radius.
[d] Disk scale length $R_D$ determined from the $V$-band image surface photometry from Herrmann et al. (2013). In the case of galaxies with breaks in their surface brightness profiles, we have chosen the scale length that describes the primary underlying stellar disk.
[e] Break radius $R_{Br}$ where the $V$-band surface brightness profile changes slope given by Herrmann et al. (2013). DDO 47 and DDO 210 do not have breaks in their surface brightness profiles.
[f] SFR measured from the integrated FUV luminosity and normalized to the area within one $R_D$ from Hunter et al. (2010). The normalization is independent of the radial extent of the FUV emission in a galaxy.

(AIPS) and then smoothed it to the H I beam using SMOTH in AIPS. We also blanked the pixels outside of the galaxy FUV emission, replacing the blanked pixels with zeros, so that pure noise would not add to the correlation coefficient $C_{coef}$. We constructed the KED maps as $0.5 \times N_{HI} \times v_{disp}^2$, where $N_{HI}$ is the H I column density in hydrogen atoms per cm$^2$ and $v_{disp}$ is the velocity dispersion in km s$^{-1}$. The conversion from counts in the KED maps to ergs pc$^{-2}$ is given for each galaxy in Table 2. Prior to executing the cross-correlations, we scaled both the FUV and KED images so that the pixel values were the same order of magnitude (roughly 100). These KED values determined from H I column density have not been multiplied by 1.36 to include helium and heavy elements. This factor will

be used later when the efficiency of KED generation is calculated.

We decided not to remove the underlying exponential disks for the 2D cross-correlations. Although the SFR drops off with radius, the FUV image consists of knots of young stars, and there can be large FUV knots in the outer disks. For the H I moment 0 and 2 maps, the H I surface density and velocity dispersion do, on average, change with radius, too, but not in a regular and homogeneous fashion. Thus, in the 2D $C_{coef}$ maps exponential structure could remain.

Here, a $C_{coef}$ of 1 is perfectly correlated such that every bump and wiggle in one map is exactly reproduced in the other. A value of −1 is perfectly anticorrelated. The amplitude of the

**Table 2**
Correlation Coefficients and Offsets

| Galaxy | Max $C_{coef}$ | X Shift[a] | Y Shift[a] | Shift/$R_D$ | Offset $(X \times Y)$[b] | Calibration $(10^{41})$[c] |
|---|---|---|---|---|---|---|
| CVnIdwA | 0.77 | 3 | 2 | 0.38 | 75 × 75 | 7.67 |
| DDO 43 | 0.61 | 4 | 13 | 0.89 | 150 × 150 | 18.33 |
| DDO 46 | 0.57 | −5 | −9 | 0.40 | 150 × 150 | 26.77 |
| DDO 47 | 0.54 | 2 | −4 | 0.13 | 150 × 150 | 9.32 |
| DDO 50 | 0.41 | −2 | −8 | 0.14 | 300 × 300 | 20.40 |
| DDO 52 | 0.56 | 6 | −14 | 0.91 | 150 × 150 | 24.86 |
| DDO 53 | 0.58 | −4 | 5 | 0.36 | 150 × 150 | 24.54 |
| DDO 63 | 0.41 | 8 | −5 | 0.39 | 150 × 150 | 18.81 |
| DDO 69 | 0.50 | −15 | −9 | 0.54 | 150 × 150 | 28.29 |
| DDO 70 | 0.50 | −23 | 18 | 0.63 | 300 × 300 | 4.83 |
| DDO 75 | 0.52 | −8 | −2 | 0.43 | 300 × 300 | 18.09 |
| DDO 87 | 0.48 | −2 | 2 | 0.09 | 150 × 150 | 18.73 |
| DDO 101 | 0.59 | −15 | 5 | 0.76 | 150 × 150 | 15.22 |
| DDO 126 | 0.62 | 2 | 3 | 0.15 | 150 × 150 | 22.95 |
| DDO 133 | 0.65 | 1 | 2 | 0.05 | 150 × 150 | 6.61 |
| DDO 154 | 0.50 | 10 | −4 | 0.60 | 150 × 150 | 17.69 |
| DDO 167 | 0.72 | 9 | 11 | 1.97 | 150 × 150 | 22.95 |
| DDO 168 | 0.68 | −2 | 0 | 0.08 | 150 × 150 | 19.36 |
| DDO 187 | 0.74 | −8 | 0 | 0.35 | 150 × 150 | 25.58 |
| DDO 210 | 0.63 | 23 | 1 | 0.94 | 150 × 150 | 8.77 |
| DDO 216 | 0.63 | 20 | 15 | 0.90 | 75 × 75 | 3.54 |
| F564-V3 | 0.87 | 0 | −4 | 0.40 | 150 × 150 | 8.69 |
| IC 1613 | 0.33 | 1 | 2 | 0.02 | 300 × 300 | 17.69 |
| LGS 3 | 0.46 | 13 | −19 | 0.73 | 150 × 150 | 8.05 |
| M81dwA | 0.42 | −11 | −16 | 1.88 | 150 × 150 | 18.01 |
| NGC 1569 | 0.40 | 30 | 6 | 1.65 | 300 × 300 | 29.08 |
| NGC 2366 | 0.30 | −6 | −4 | 0.09 | 150 × 150 | 21.51 |
| NGC 3738 | 0.48 | −13 | 7 | 0.68 | 150 × 150 | 25.50 |
| NGC 4163 | 0.62 | 4 | 12 | 0.83 | 150 × 150 | 15.46 |
| NGC 4214 | 0.35 | −88 | 8 | 2.57 | 300 × 300 | 18.17 |
| SagDIG | 0.51 | −7 | 15 | 0.97 | 75 × 75 | 1.84 |
| WLM | 0.33 | 0 | −32 | 0.20 | 150 × 150 | 22.95 |
| Haro 29 | 0.63 | −21 | −1 | 2.69 | 150 × 150 | 23.19 |
| Haro 36 | 0.34 | −46 | −54 | 4.75 | 150 × 150 | 21.91 |
| Mrk 178 | 0.60 | 2 | −1 | 0.33 | 150 × 150 | 25.98 |
| VIIZw403 | 0.68 | 1 | −3 | 0.19 | 150 × 150 | 12.11 |

**Notes.**
[a] Offset of the pixel with the maximum $C_{coef}$ from the center of the array, in pixels. The pixel scale is $1\rlap{.}''5$ except for DDO 216 and Sag DIG, where it is $3\rlap{.}''5$.
[b] Offsets in pixels.
[c] Constant by which to convert counts in KED maps to ergs pc$^{-2}$.

peak is a measure of the coincidence of features in each image. If the KED image correlates well with the local FUV flux, then the peak will be high and the breadth will be the average size of their rms summed feature sizes.

We used the commands CORREL_IMAGES and CORRMAT_ANALYZE in IDL with a Python wrapper. We used this command to shift one image relative to the other over and over again to yield a map of $C_{coef}$. The peak pixel value in the $C_{coef}$ map is the adopted $C_{coef}$. For example, for NGC 2366, we did a 150 × 150 array of offsets. That is, we calculated the $C_{coef}$ for $x$, $y$ offset of −150, −150 to $x$, $y$ offset of +150, +150. This produces a matrix of 301 × 301 pixels. The peak, in this case, is at pixel 145, 147 and has a value of 0.3 compared to the center pixel 151, 151 value of 0.26. Thus, the maximum correlation is achieved when the FUV image is shifted relative to the KED image by the offset corresponding to $x$, $y$ of 145, 147. We checked the $C_{coef}$ of a piece of one of the galaxies "by hand" with a Fortran program we wrote, and we obtained the same peak $C_{coef}$. The peak $C_{coef}$ and $x$, $y$ shifts to that pixel are

given in Table 2. The cross-correlation matrices are shown in Figure 1.

The shift in $x$, $y$ is also given in Table 2 relative to the disk scale length $R_D$, for better comparison to the size of the galaxy. The shifts vary between $0.02R_D$ (IC 1613) and $4.75R_D$ (Haro 36). Fifty percent of the galaxies (18) have shifts less than $0.5R_D$, 33% (12) have shifts between $0.5R_D$ and $1R_D$, and 17% (6) have shifts greater than $1R_D$.

I. Bagetakos (private communication) examined the cross-correlation method on NGC 2403 as a function of image scale, focusing on scales of 0.23 to 3 kpc, and found correlations on various scales for different images such as star formation tracers, dust, and H I. Thus, we divided our images into square subregions of 16 × 16, 32 × 32, 64 × 64, and 128 × 128 pixels and computed the $C_{coef}$ in each box. The coefficient images constructed from this just look like noise and show no particular connection to the FUV image. So, we do not consider them further.

We also applied alternate methods on one galaxy, NGC 2366 with a max $C_{coef}$ of 0.3, to examine the robustness of our
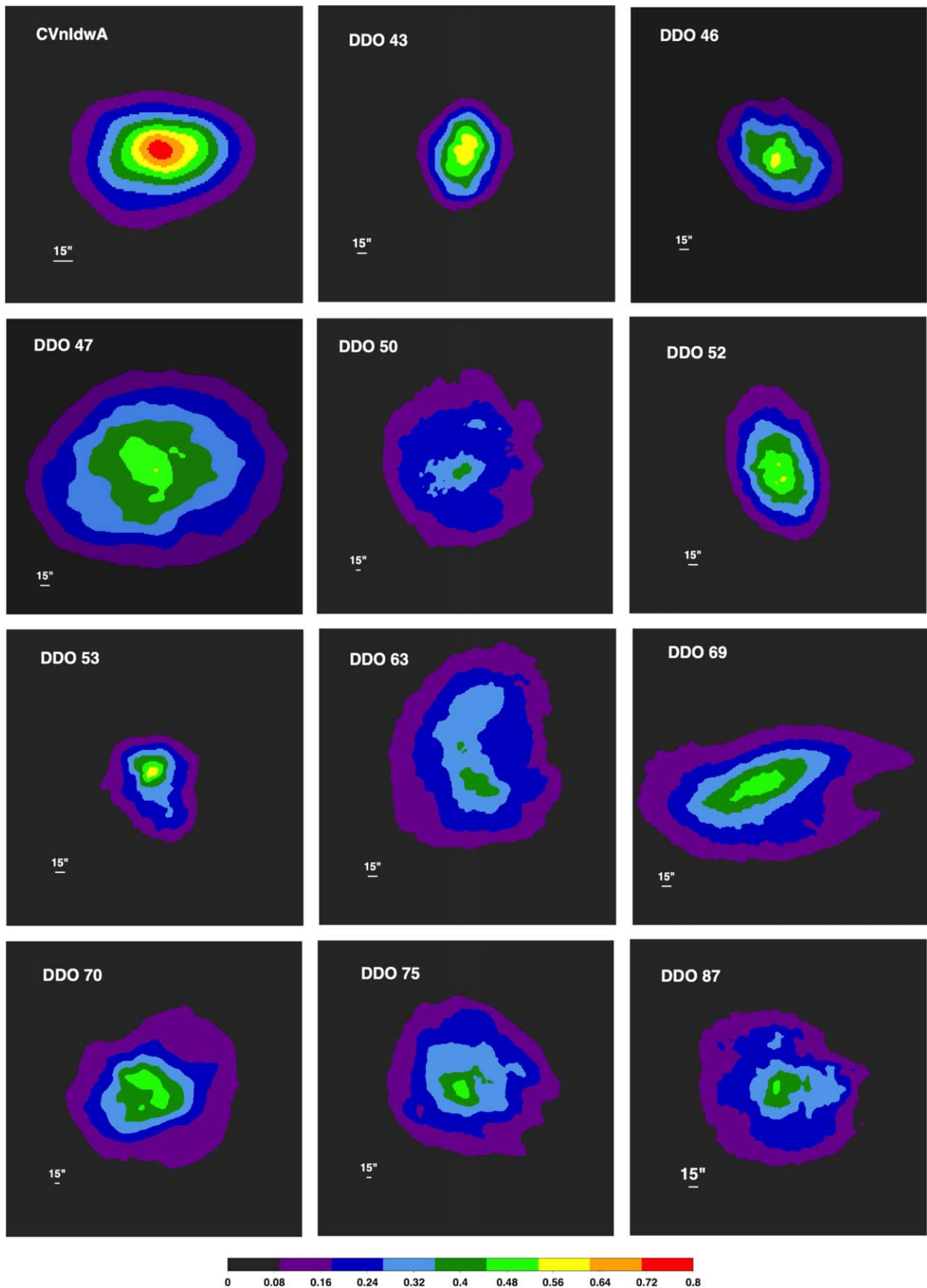
**Figure 1.** Cross-correlation matrices for each galaxy. The images are displayed with the same color scale from $C_{coef}$ of zero to 0.8.
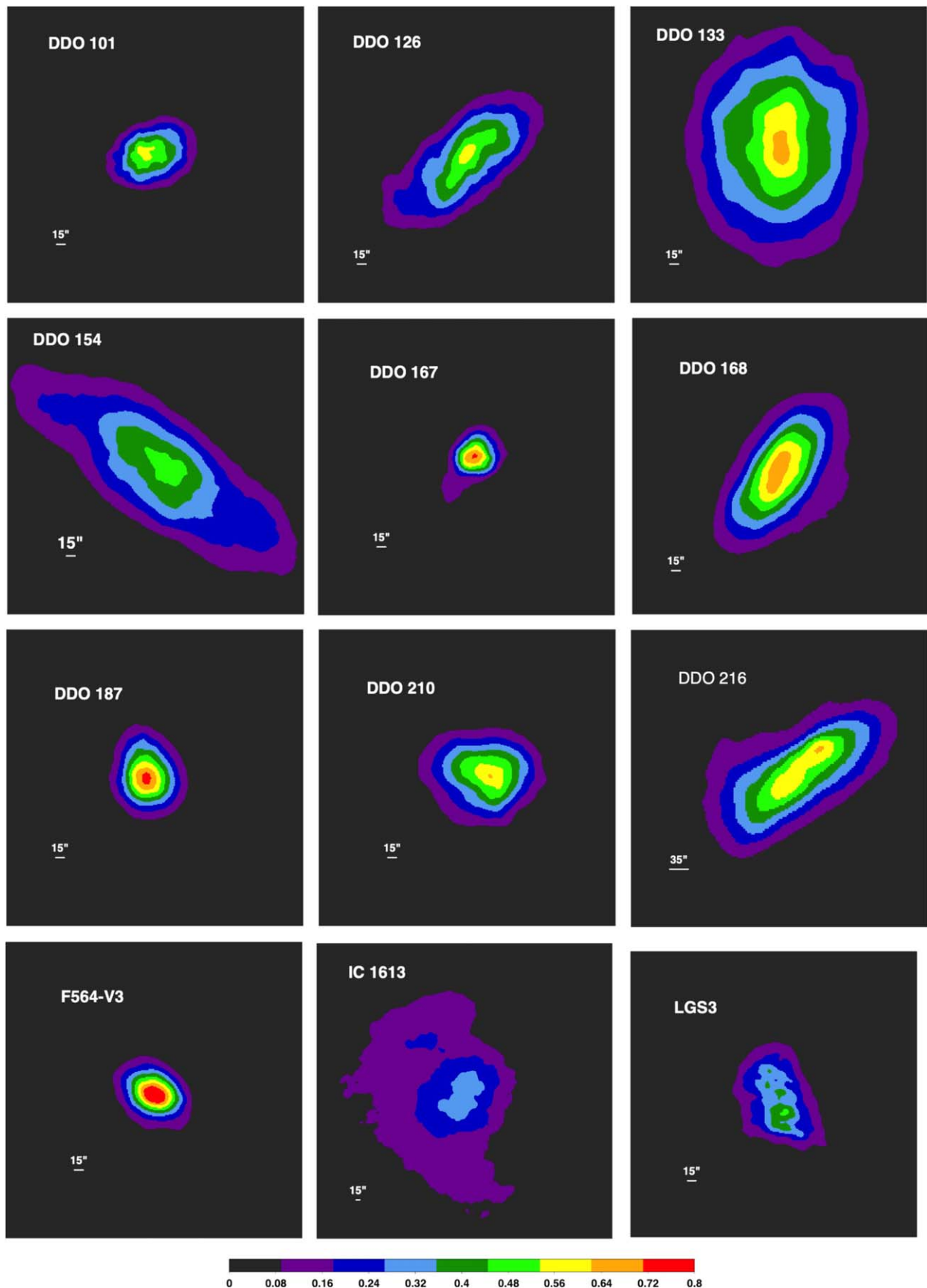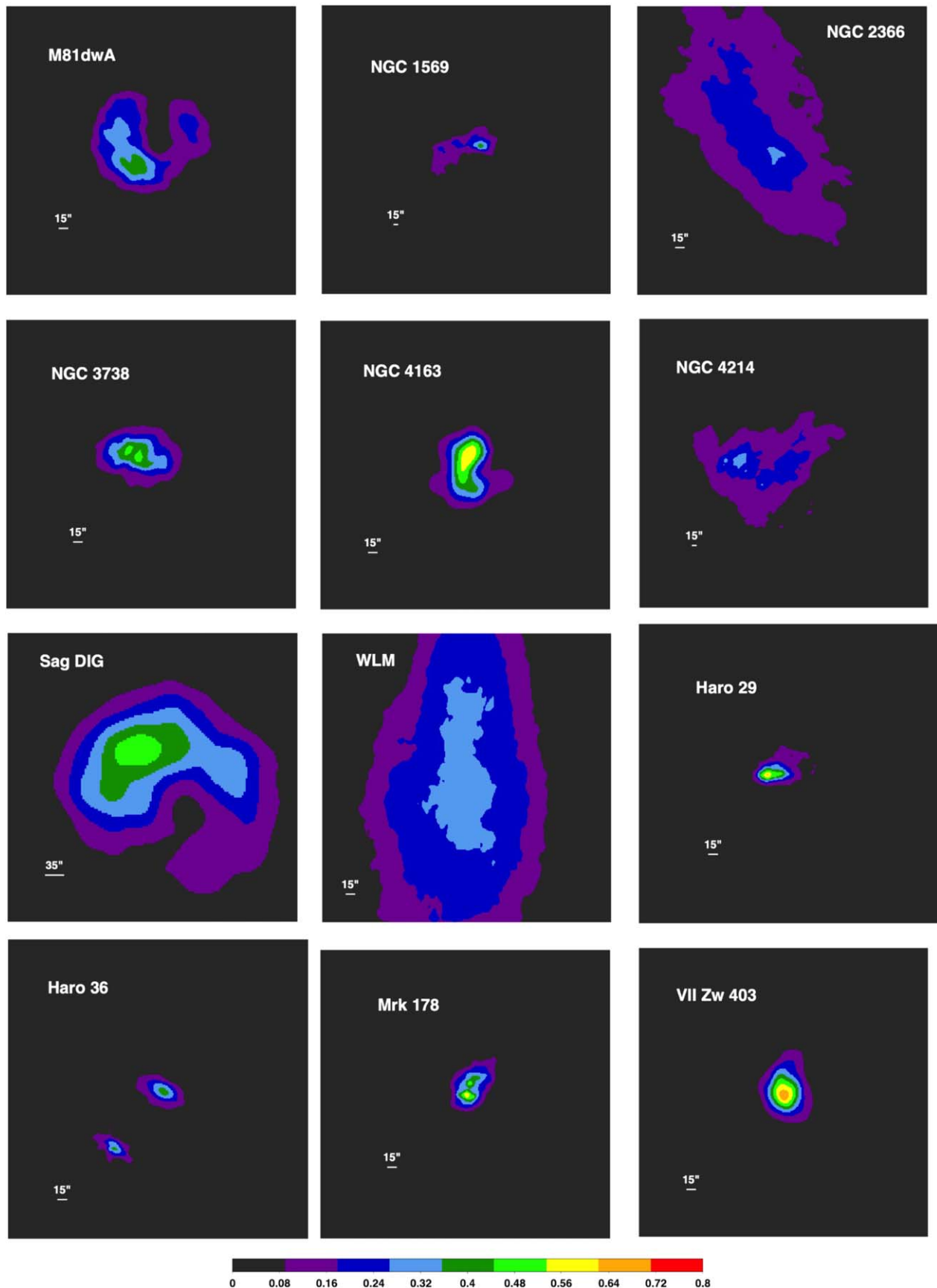
**Figure 1.** (Continued.)
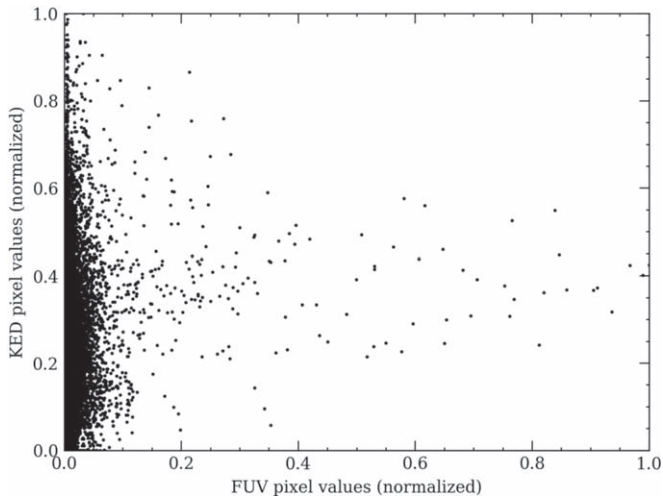
**Figure 1.** (Continued.)

**Figure 2.** Values of pixels in the KED image plotted against values of pixels in the FUV image for NGC 2366. The images have each been normalized so that pixel values are between 0 and 1. A notable correlation would be expected to appear as a cluster of points in the top-right corner (or, in the other corners near values of 1.0 for anticorrelation), however, this evidence is not seen.



**Figure 3.** Cross-correlation coefficient $r_w$ for the NGC 2366 KED and FUV images convolved with progressively larger "Mexican hat" kernels. We find no significant correlation between the two images at any resolved scale.

approach. This galaxy was chosen for initial and special tests because it has a giant H II region and the H I velocity dispersion is high around this region, making it an interesting candidate for looking for a star formation–turbulence correlation. One problem with cross-correlations, in particular, can be caused by moderate signal-to-noise ratio (S/N) pixels dampening the value of $C_{\mathrm{coef}}$. One simple diagnostic is a plot of the pixel values of the KED image against the pixel values of the FUV image, given that the FUV image has been geometrically transformed and smoothed to the same pixel grid and beam size as the KED image. We normalized the pixel values in each image to range from 0 to 1, and this plot is shown in Figure 2. If there were a notable correlation, we would expect a cluster of points in the top-right corner. If the images were anticorrelated, we would expect clusters of points around the top left and bottom right. We do not see either of these extremes. While there are some points in the top-left corner, it is not a distinct cluster; rather, it appears to be consistent with the typical tail end of a simple distribution of points from 0 to 1.

We also tried variations of the weighted normalized cross-correlations (WNCCs) and a wavelet analysis to NGC 2366. The zero-mean normalized cross-correlation coefficient (ZNCC) is basically the standard Pearson correlation measure $\rho$ for a 2D image. Applied to NGC 2366, ZNCC is 0.26. Like $\rho$ or $r$ coefficients, $+1$ is perfect correlation, $-1$ is perfect anticorrelation, and so 0.26, which is what we found for the max $C_{\mathrm{coef}}$, implies a not very significant degree of correlation. One way to deal with pixels with low S/N is to use a WNCC. For this test, we weighted the pixels by the ratio of their signal to the standard deviation of values in the map, which is effective at downweighting background noise pixels. Using this method, we obtain a WNCC value of $-0.023$—effectively zero, implying no significant correlation between the two images.

For our final test on NGC 2366, we used a wavelet analysis to see if the degree of correlation depends on scale/resolution. In this process, each image is convolved with progressively larger 2D kernels or wavelets, in this case, a Ricker or "Mexican hat" wavelet, and the cross-correlation is calculated
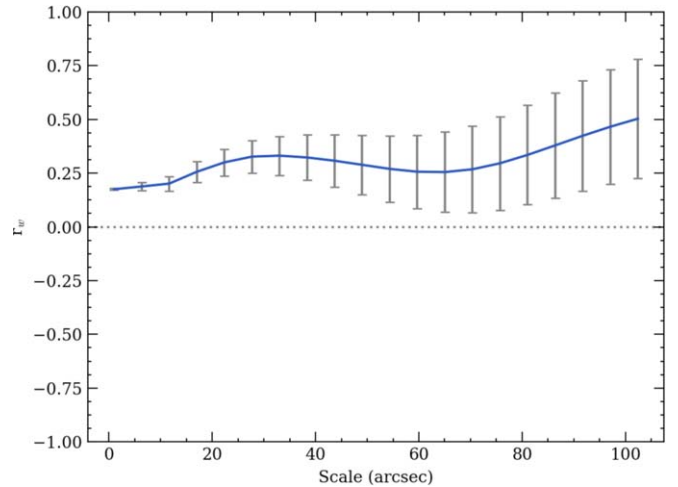
at each of these scales or "lags." The result for NGC 2366 is shown in Figure 3. Strong correlations at a particular spatial scale would be evidenced by wavelet cross-correlation $r_w$ values of $\gtrsim 0.6$ at that scale. Eventually, as the images are convolved to large-enough scales, they become less resolved and therefore naturally correlate. Figure 3 indicates that there is not much difference at any of the resolved scales. Using a slightly modified wavelet from the literature (e.g., Ossenkopf et al. 2008), there may be evidence of a slightly more prominent correlation between the images at 30 pixel scales (45″), but $r_w$ is still not significant.

Thus, we conclude that no matter how we look at the FUV and KED images of NGC 2366, the two images are mildly correlated at best, and this does not change much with scale.

The width of the peak signal in a cross-correlation matrix is expected to represent the scale of the correlation. However, in our matrices, the width is not well defined. The issue is demonstrated in Figure 4 where we show a radial plot and row and column cuts through the peak of the WLM $C_{\mathrm{coef}}$ matrix. The peak is, of course, obvious, but the radial plot is messy and the single row and column cuts show a complex background. The main feature in the cross-correlation maps is the exponential disk because both the KED and the SFR density peak in the center with the exponential disk. The width of the $C_{\mathrm{coef}}$ in Figure 4 is influenced more by the width of the disk than the scale of the 2D correlation. What to take as the baseline for a fit to the peak is also not clear. Therefore, we do not consider the widths of the peaks further here.

### 3.2. Radial Profiles

We also calculated the $C_{\mathrm{coef}}$ in annuli from the center of the galaxy outward. The image was blanked outside of the target annulus, which was chosen to match those used by Hunter et al. (2012) to produce the H I radial profiles. We normalized the pixel values in the annulus with respect to the average in the annulus, so in effect large-scale variations, such as the exponential falloff with radius, are taken out. Then, we measured the $C_{\mathrm{coef}}$ for the annulus. Figure 5 shows the $C_{\mathrm{coef}}$ of the annuli as a function of the annulus distance from the
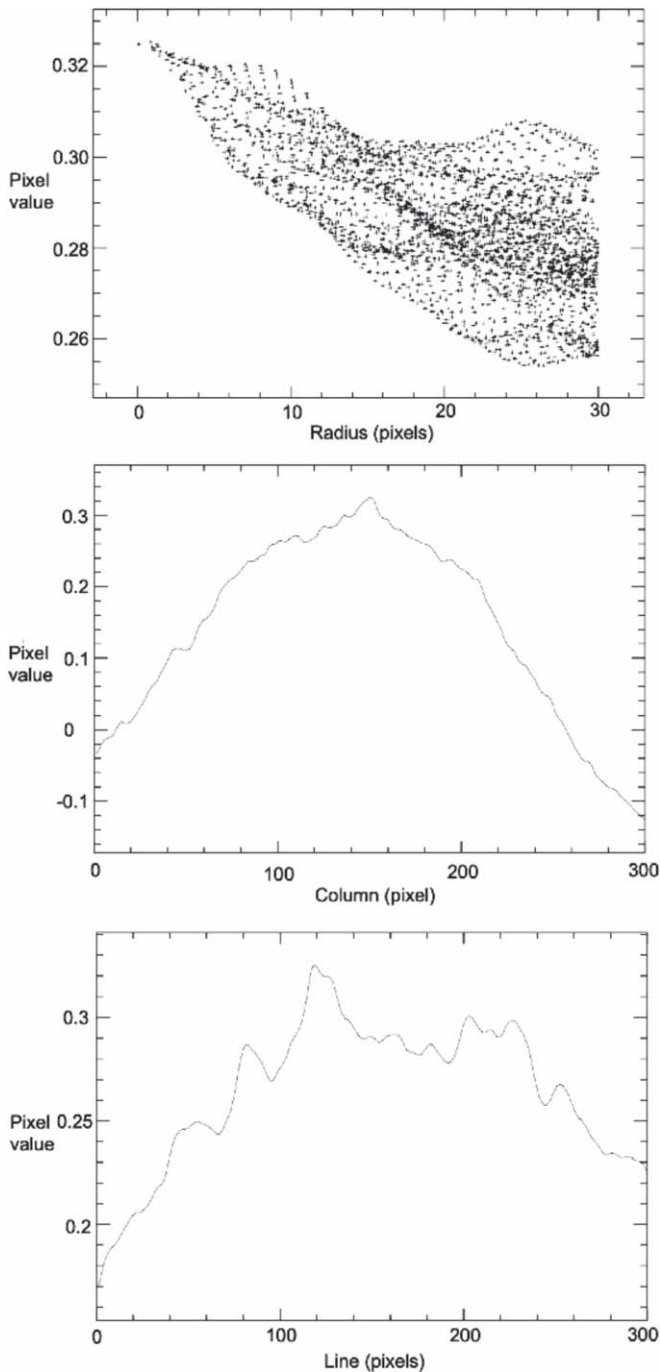
## 4. Results

### 4.1. Cross-correlations

Generally, the 2D $C_{coef}$ indicates low levels of correlation between the FUV and KED images. In Figure 6, we plot the peak $C_{coef}$ against the integrated SFR for each galaxy to see if a higher level of correlation is related to the overall SFR. There is no relationship between the two values. In annuli, $C_{coef}$ can be as high as 0.9 in the center, indicating a correlation, but the values tend to be low overall, and the radial profiles exhibit a wide range of shapes. From the images, visually, most of the FUV is patchy and tends to be concentrated toward the central regions of the galaxies while the H I often extends quite far outside the optical/UV galaxy. So, the bird's eye view of a dIrr might expect a higher correlation in the central regions where there is ample H I and FUV, with little correlation as you go farther out where there are typically fewer FUV knots.

By comparison, in the spiral NGC 2403, I. Bagetakos (private communication) found that the FUV and H I surface mass density are uncorrelated with a $C_{coef} < 0.20$. They did, however, find correlations between dust and star formation ($C_{coef} > 0.55$) and between PAHs and H I ($C_{coef} \sim 0.55$). Bagetakos et al. chose NGC 2403 as their pilot galaxy because it is in the THINGS sample (Walter et al. 2008) with H I data, as well as images at 8 $\mu$m, 24 $\mu$m, H$\alpha$, and FUV, and is nearby with a H I beam of 136 pc × 119 pc. As an Scd spiral, it is significantly larger and more massive than the dIrr galaxies in this study.

### 4.2. Degree of Lumpiness

Because star formation is usually lumpy, we ask whether the lack of correlation between FUV and KED images is because KED is smooth compared to FUV or because the lumps in the two images do not correlate. Figure 7 shows the KED maps and FUV images at full resolution. A contour of the FUV image is superposed on the KED map to facilitate comparison. We see that the FUV and KED maps are both generally lumpy, although the lumps are not necessarily located in the same place.

To examine the degree of lumpiness, we looked at the fraction of pixels with raw values above a given percentage of the maximum pixel value in the image. Specifically, we counted the fraction of total pixels that have counts within 10%, 20%, 30%, 40%, and 50% of the maximum count value in each of the FUV and KED images. These data are shown in Figure 8 as a percentage of total pixels as a function of selected cutoff deviation from the maximum pixel value in the image. For example, in CVnIdwA, the percentage of pixels with values within 10% of the maximum value is 0.69% in the FUV image and 1.03% in the KED image, whereas the percentage of pixels with values within 50% of the maximum value is 5.65% in the FUV image and 15.98% in the KED image.

To understand what these plots mean, we can compare the appearance of the galaxies in Figure 7 with the plots in Figure 8. We see in the images that galaxies like LGS 3, DDO 87, DDO 133, and SagDIG have a few small FUV knots but more or bigger KED knots. The KED knots fill more of the area and so a higher fraction of the pixels are close to the peak intensity. These galaxies have flat FUV profiles in Figure 8 because very few pixels are close to the peak intensity, i.e., the FUV is spotty, but they have KED profiles that increase with the percentage of the maximum pixel value because the KED is
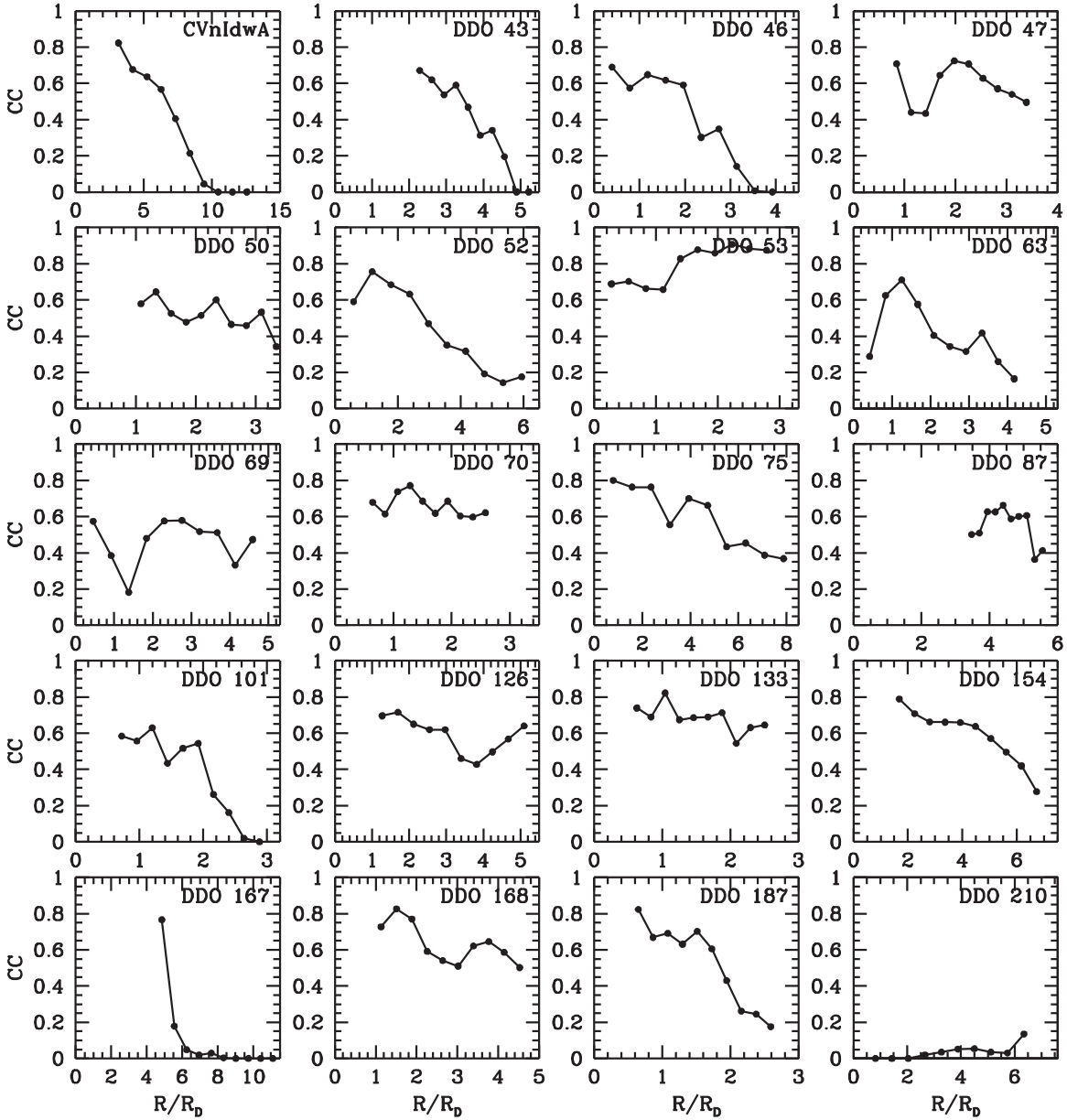


**Figure 4.** Cuts through the peak in the $C_{coef}$ matrix of WLM. Top: radial profile. Middle: row plot. Bottom: column plot.

center of the galaxy. The annuli used the galaxy center, ellipticity, and major axis position angle determined from V-band images and given by Hunter et al. (2012).

We see a wide variety of profiles. The central points in NGC 4163 and in VIIZw403 reach a $C_{coef}$ of nearly 0.95, and a few other galaxies have peaks as high as 0.9. By contrast, the peak in DDO 210 occurs in the outermost annulus and only reaches a value of 0.14. In many galaxies, the $C_{coef}$ drops in value with radius, but in many others, it is relatively flat. In a few galaxies, the $C_{coef}$ drops precipitously from a relatively high value for the innermost annulus to near zero beyond that radius (DDO 167, F564-V3, Haro 36).

**Figure 5.** Correlation coefficient between FUV and KED images in annuli as a function of distance from the center of the galaxy. The $C_{coef}$ profile is plotted from 0 to 1 for all galaxies for ease of comparison, and the radius is normalized by the disk scale length measured from the *V*-band image (Table 1). The pixel values in each annulus have been normalized by the average in the annulus, so large-scale trends with radius have been removed.

more uniform. DDO 43 is unique in this sample because it is the only one with an approximately flat KED profile and an FUV profile that increases with the percentage of the maximum pixel value. The reason is clear from Figure 7, which shows that the FUV image of DDO 43 is filled with bright spots, making most of the image close to the peak pixel value, while the KED image has weaker peaks that are more spread out. DDO 167, on the other hand, has FUV and KED knots that are comparable in size, and FUV and KED profiles that increase together with the percentage of maximum pixel value, as do DDO 47, DDO 101, F564-v3, and NGC 4163. Most of the galaxies have broader KED distributions than FUV emission, so their KED pixel percentages increase faster than their FUV pixel percentages as the top percentage of the maximum pixel value increases.

The general increasing trend of the curves in Figure 8 is mostly the result of the exponential radial profile of the disk,

with the peaks in KED and FUV standing for a nearly fixed fraction above the mean profile. Figure 9 shows the models for these curves assuming an exponential disk intensity profile $I(r) = e^{-r}$, so the radius as a function of intensity is $r(I) = -\ln(I)$. The radius at 10% of the peak is then $r(10\%) = -\ln(1 - 0.1)$, and the number of pixels brighter than that is the area of the circle at this radius, or $\pi r(10\%)^2$. In general, for an intensity that is a fraction $x$ down from the peak intensity, the fraction of pixels in the total disk is

$$f(x) = \pi(-\ln[1 - x])^2 / (\pi r_{max}^2), \quad (1)$$

where $r_{max}$ is the size of the disk measured in scale lengths. Figure 9 shows $f(x)$ versus $x$ in three cases. The top curve is for an exponential profile with a scale length 1.5 times larger than the middle curve and an overall galaxy size that is the same, $r_{max} = 2$ scale lengths. The lower curve also has a scale length

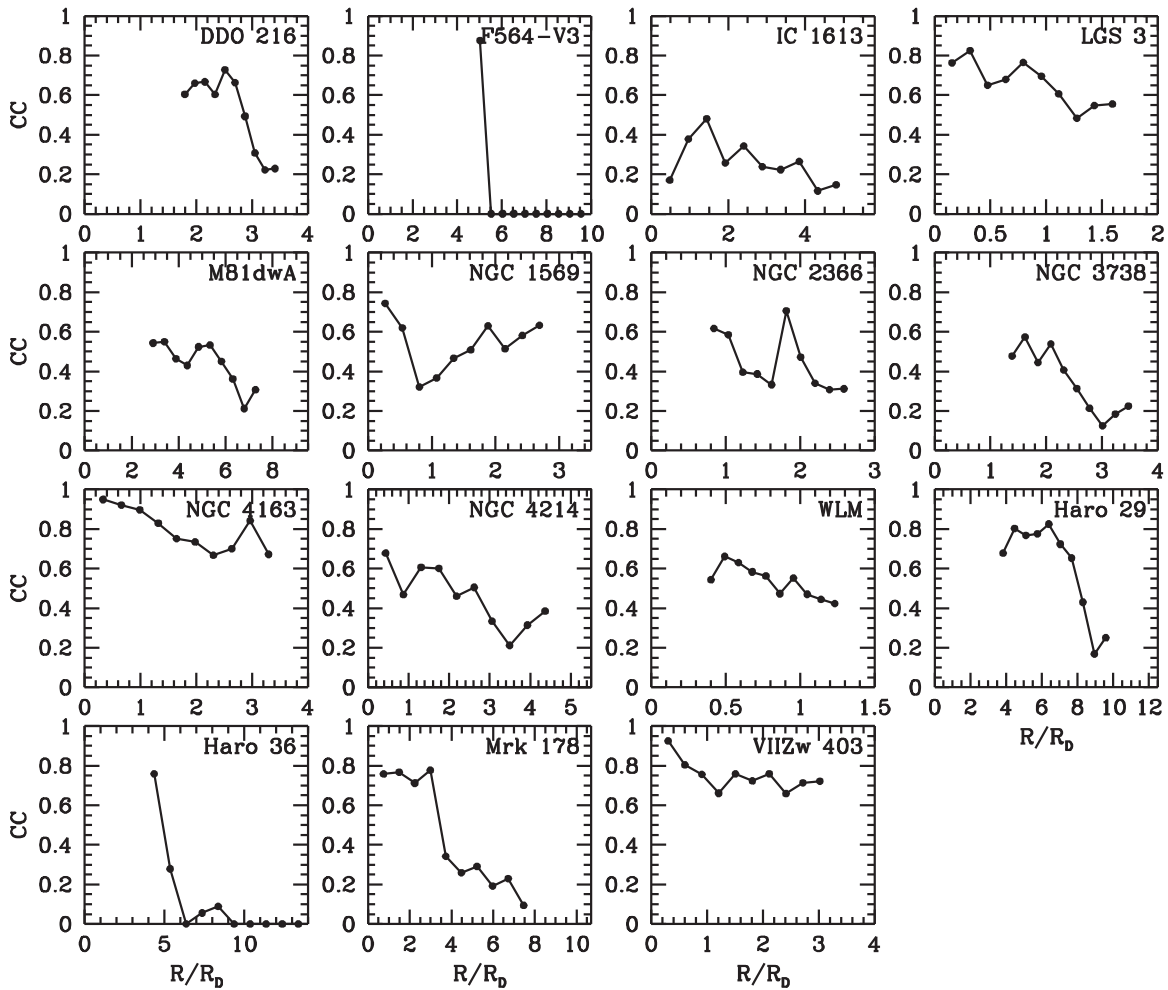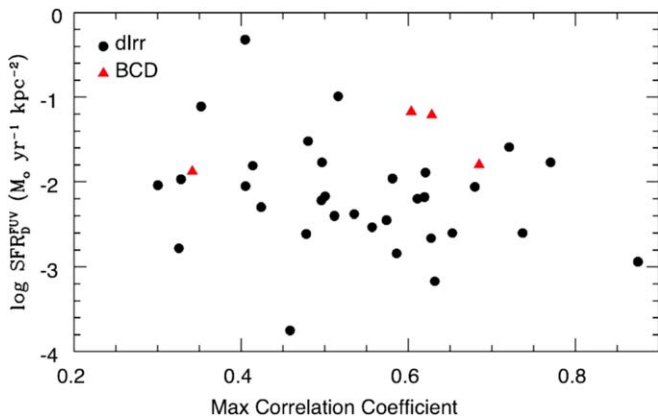**Figure 5.** (Continued.)



**Figure 6.** Integrated SFR normalized to one disk scale length vs. the maximum correlation coefficient for each galaxy. The correlation coefficients are given in Table 2 and the SFRs are in Table 1.

1.5 times larger than the middle curve, but the overall galaxy size for the lower curve is 1.5 times larger ($r_{max} = 3$). Larger scale lengths for a given galaxy size make the percentage curves rise faster because more of the disk is close to the peak intensity at the center.

The similarity of the model curves in Figure 9 to the observations in Figure 8 implies that the qualitative effect

being captured by the fractional distribution is the result of the exponential disk. However, the percentage of pixels observed is much smaller than the model percentage, i.e., several percent or less for the observations compared to $\sim 10\%$ at the 50% top percentage of the maximum pixel value. This difference implies that the peaks in the KED and FUV distributions stand above the exponential disk, so their areas are a small fraction, $\sim 10\%$, of the disk area, but the peak intensities have about the same radial dependence as the average disk, which means they are a fixed factor times the average disk brightness.

### 4.3. Pixel–Pixel Scatter Plots

Another way of looking at the data is to compare individual pixels in pairs of images. We have done that, examining KED, the velocity dispersion of the gas $v_{disp}$, and H I surface density $\Sigma_{HI}$ versus SFR surface density as determined from the FUV images, $\Sigma_{SFR}$. Recall that the FUV images were geometrically transformed and smoothed to match the pixel size and resolution of the H I images. For all galaxies but DDO 216 and Sag DIG, the pixel size is 1.5″, and for these two, it is 3.5″. To compensate for radial trends, we determined the azimuthally averaged $\Sigma_{SFR}$, KED, H I, and $v_{disp}$ in annuli from the center of the galaxy and subtracted that from the observations. We used optically determined disk parameters of the center, minor-to-
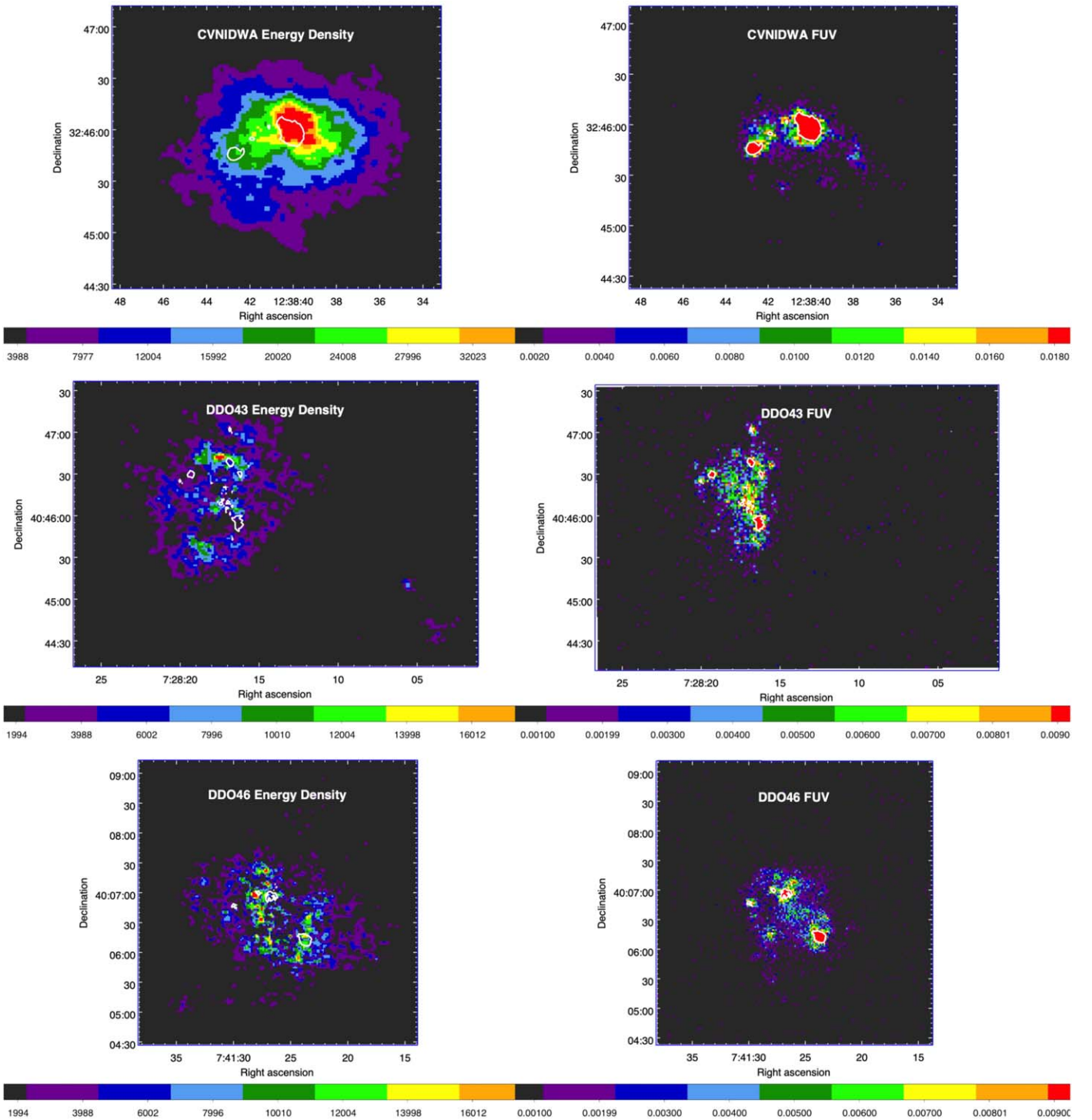
**Figure 7.** Kinetic energy density (KED) maps and full-resolution FUV images for each galaxy. The major FUV knots are contoured and the white contour is shown on the KED map to facilitate comparison. The conversion of counts in the KED maps to physical units is given in Table 2. To convert FUV counts s$^{-1}$ to flux in units of erg s$^{-1}$ cm$^{-2}$ Å$^{-1}$, multiply by $1.4 \times 10^{-15}$. Figures for the rest of the galaxies in this study are available in the online materials (72 images in 12 figures). (An extended version of this figure is available.)

major axis ratio $b/a$, and position angle of the major axis from Hunter et al. (2012). The widths of the annuli, constant in a given galaxy, were chosen to be the same as those used to measure the H I surface density profiles of Hunter et al. (2012). The azimuthally averaged radial profiles of $\Sigma_{SFR}$, KED, $v_{disp}$, and $\Sigma_{HI}$ are shown for each galaxy in Figure 10. The pixel–pixel plots of the excess KED, $v_{disp}$, and $\Sigma_{HI}$ versus excess

$\Sigma_{SFR}$ are shown in Figures 11–13. All of these quantities except $v_{disp}$ were corrected to a face-on orientation by multiplying the fluxes by the cosine of the inclination. The KED units are erg pc$^{-2}$, $v_{disp}$ is in km s$^{-1}$, $\Sigma_{HI}$ is in $M_\odot$ pc$^{-2}$, and $\Sigma_{SFR}$ is in units of $M_\odot$ yr$^{-1}$ pc$^{-2}$. KED values in Figures 10–13 have not been corrected for helium and heavy elements. Note that only the regions of relatively high $\Sigma_{SFR}$ are
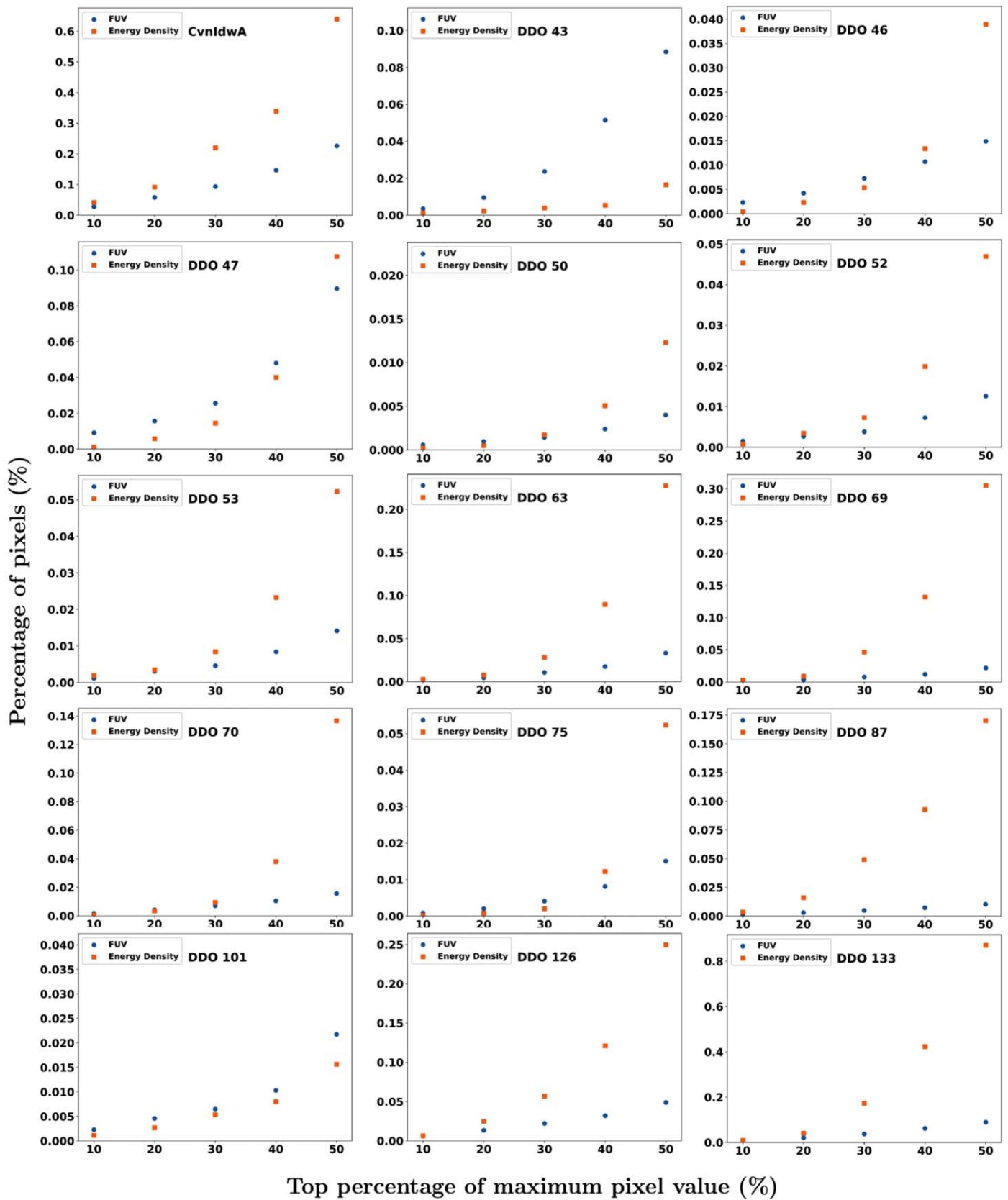
**Figure 8.** Percentage of pixels with values above a given percentage of the maximum value for FUV and KED images.

plotted, i.e., with a positive excess above the annular average, and we plot the logarithm of this excess. For the quantities on the ordinate, we consider both positive and negative excess

values over the average, so they are not plotted in the log. Some regions of locally high $\Sigma_{SFR}$ have locally low KED, $v_{disp}$, or $\Sigma_{HI}$.
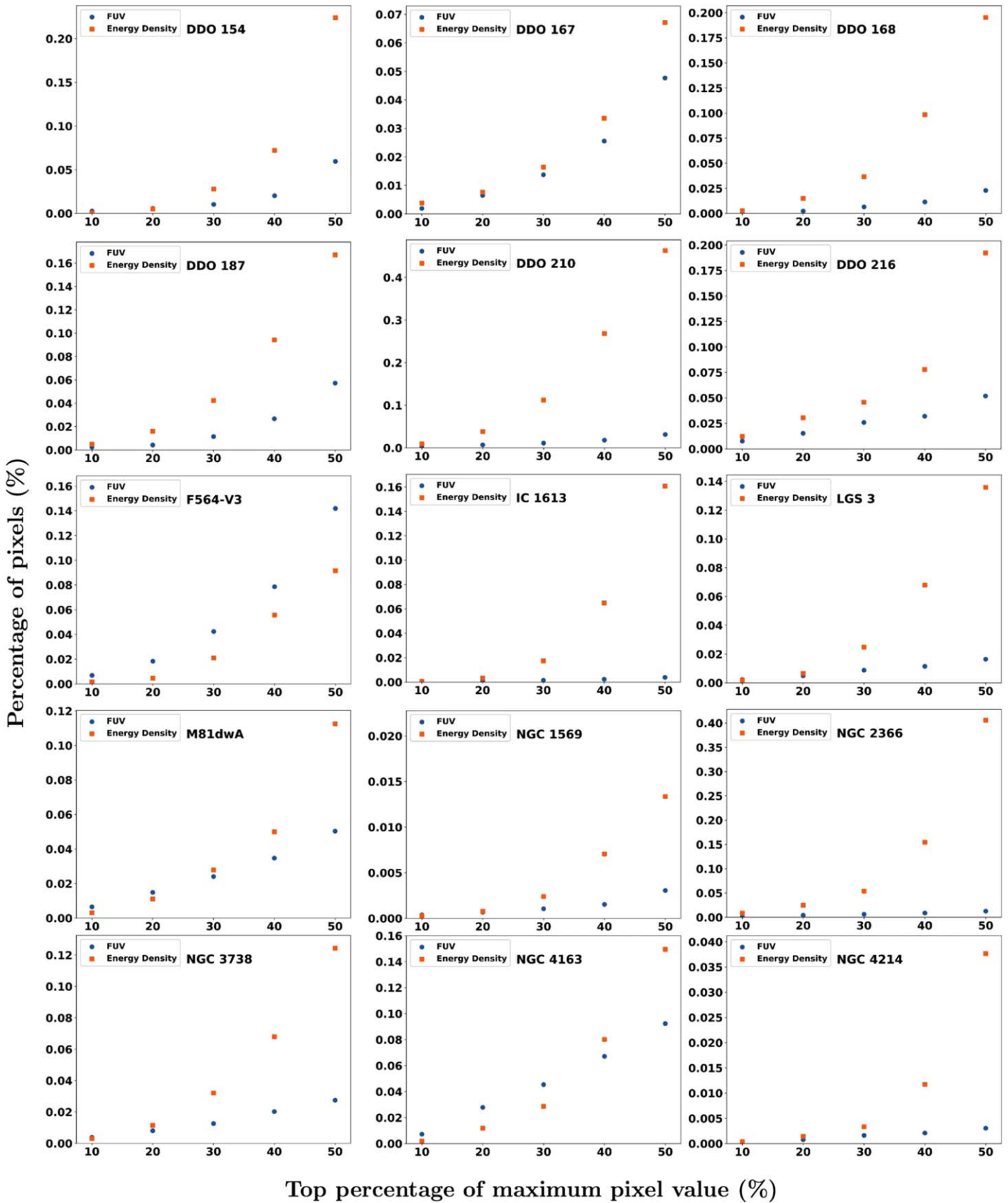
**Figure 8.** (Continued.)

In the radial averages shown in Figure 10, we see that KED, $\Sigma_{\mathrm{SFR}}$, and $\Sigma_{\mathrm{HI}}$ generally decrease with radius. Tamburro et al. (2009) found this also for spiral galaxies. They also found that $v_{\mathrm{disp}}$ decreases with radius in their sample, but in our sample of dIrr, the drop of $v_{\mathrm{disp}}$ with radius is very minor, if any. They also find a clear correlation of KED with $\Sigma_{\mathrm{SFR}}$ in pixel–pixel
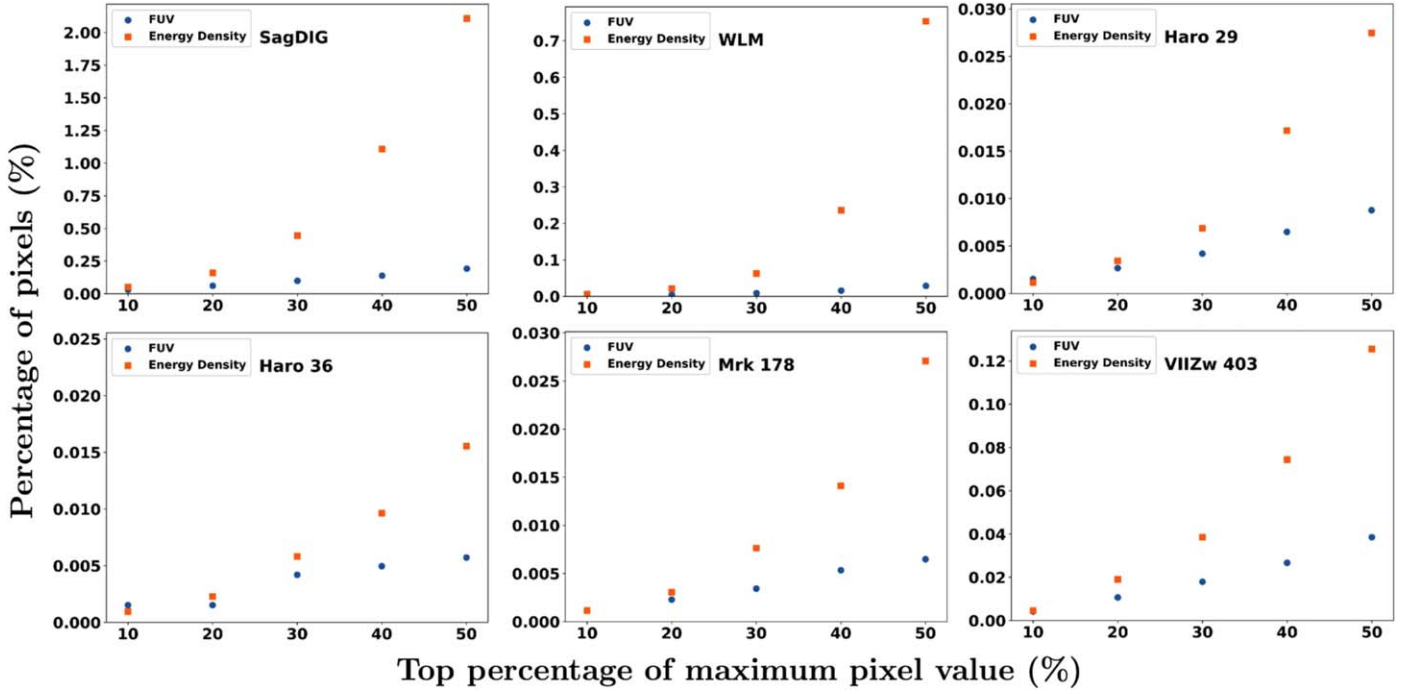
**Figure 8.** (Continued.)
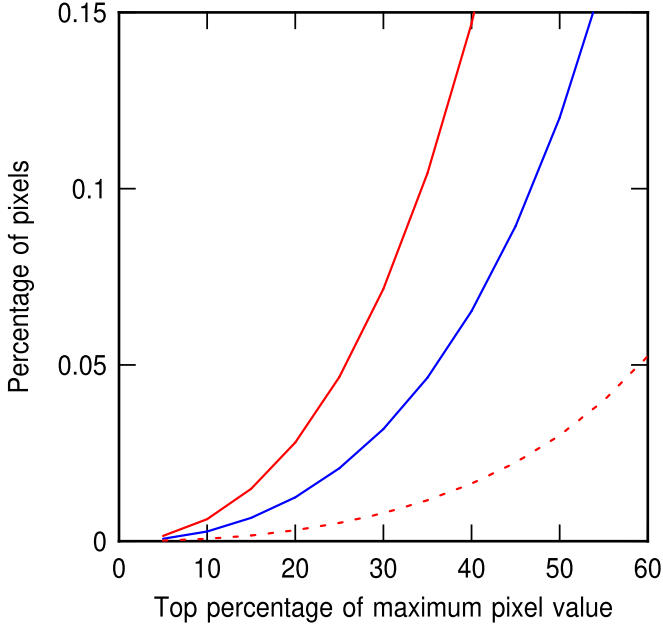


**Figure 9.** Model for the curves in Figure 8 based on exponential profiles. The top curve has a scale length 1.5 times larger than the middle curve and an overall galaxy size the same, 2 scale lengths. The lower curve also has a scale length 1.5 times larger than the middle curve, but the overall galaxy size for the lower curve is 1.5 times larger. Larger scale lengths for a given galaxy size make the percentage curves rise faster because more of the disk is close to the peak intensity at the center.

plots, whereas our Figure 11 does not show such a nice correlation.

Figures 11–13 typically show concentrations of points at a low excess $\Sigma_{SFR}$ and a continuation of these points toward higher excess $\Sigma_{SFR}$. The low excess $\Sigma_{SFR}$ is in the outer disks and the high excess $\Sigma_{SFR}$ is in the inner disks. Some galaxies have two concentrations of points in these figures.

To quantify the pixel distributions, we determined the excess $\Sigma_{SFR}$ and other quantities at the plotted concentrations. For each galaxy, we made a histogram of the log of the excess $\Sigma_{SFR}$ (the abscissa value) and found the peak at the low-density concentration. The excess log $\Sigma_{SFR}$ in that peak was determined from the average value in the three bins of the histogram centered there. The bin width was 0.2 in the log of the excess $\Sigma_{SFR}$. Then, for these three bins around the histogram peak for log excess $\Sigma_{SFR}$, we determined the mean value of the quantity plotted on the ordinate in the figures, i.e., the excess KED, $v_{disp}$, and $\Sigma_{HI}$. For the higher-excess $\Sigma_{SFR}$, we took the mean value of the excess $\Sigma_{SFR}$ and the other quantities for all regions where the log of the excess $\Sigma_{SFR}$ was larger than the high-star-formation edge of the concentration of points, typically at $-9.8$ but ranging from $-9.5$ to $-10.2$ depending on the plotted galaxy. When there was only one prominent concentration of points in the figure, we determined the values there.

Figure 14 shows the mean excess KED corrected for helium and heavy elements, $v_{disp}$, and $\Sigma_{HI}$ versus the mean of the log of the (positive) excess $\Sigma_{SFR}$ for all galaxies, with dots corresponding to the low-$\Sigma_{SFR}$ concentrations in the outer disks and crosses corresponding to the high $\Sigma_{SFR}$ in the inner disks. The curves in the KED plot show fitted relationships between the KED generated by supernovae and the $\Sigma_{SFR}$ for the indicated efficiencies of converting supernova energy into turbulence and for galaxy scale heights of 850 pc and 540 pc. These theoretical KEDs come from Equation (3.7) in Bacchini et al. (2020), which is

$$KED_{SN} = \eta \Sigma_{SFR} f_{cc} E_{SN}(2H/v_{turb}), \qquad (2)$$

where $\eta$ is the efficiency of energy conversion from supernova to turbulence, $f_{cc} = 1.3 \times 10^{-2} \, M_\odot^{-1}$ is the number of core-collapse supernovae per solar mass of stars, $E_{SN} = 10^{51}$ erg is the supernova energy, $H$ is the disk thickness, and $v_{turb}$ is the
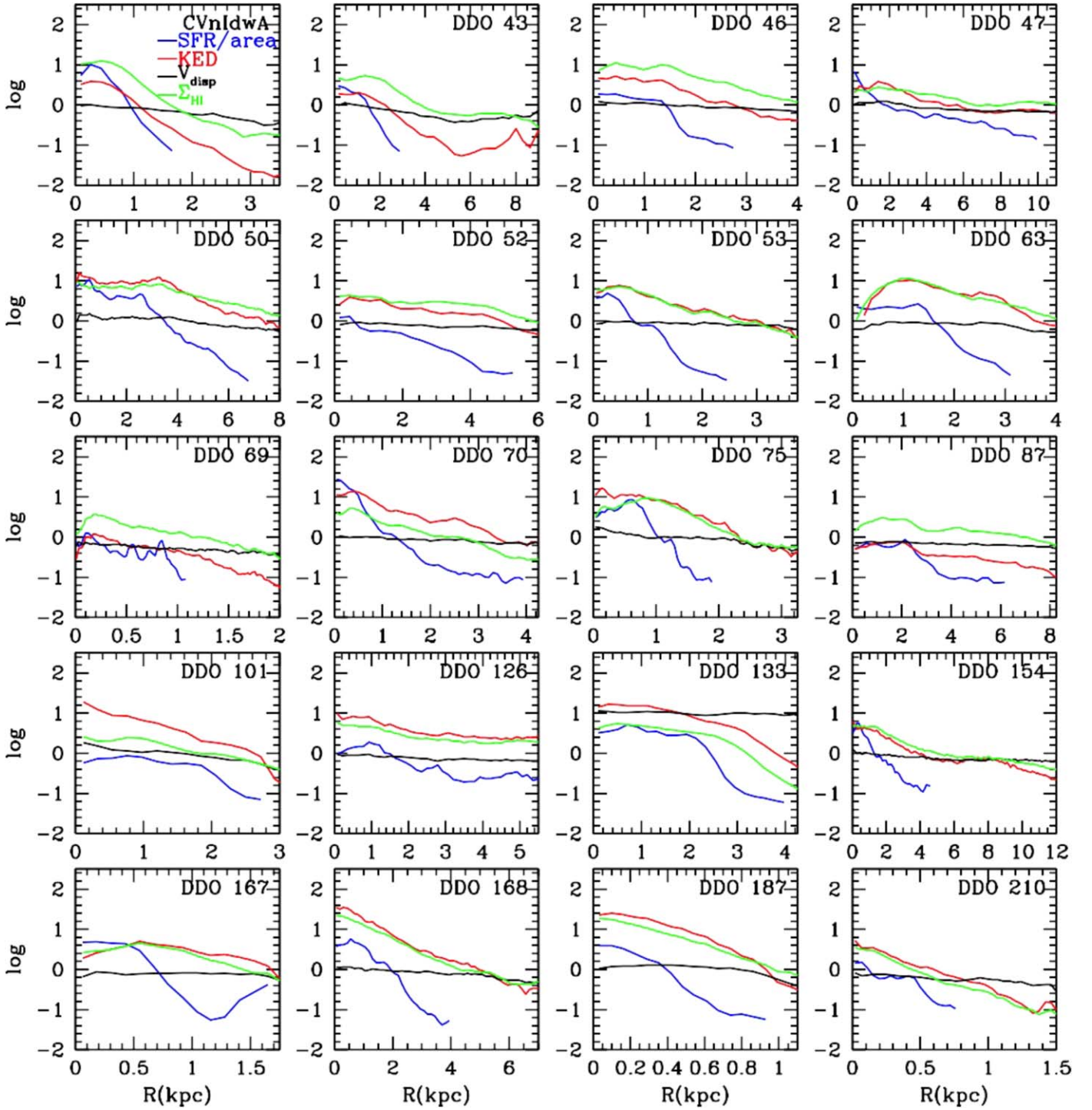
**Figure 10.** Azimuthally averaged radial profiles of $\Sigma_{SFR}$ determined from the FUV, KED (not corrected for He and heavy elements), $v_{disp}$, and $\Sigma_{HI}$. FUV emission is the limiting quantity in that it does not go out as far as the other quantities. Optical disk parameters (center, $b/a$, and major axis position angle) from Hunter et al. (2012) were used, and holes in the gas or FUV emission were not used in the averages.

turbulent gas velocity dispersion (the ratio of these latter two quantities gives the turbulent dissipation time). Bacchini et al. (2020) compare the radial profiles of turbulent energies in 10 nearby galaxies with the SFRs and derive an average efficiency of $1.5^{1.8}_{0.8}\%$ if all of the turbulence comes from star formation. Because the required efficiency is relatively low, they concluded that supernovae related to star formation can drive most of the interstellar turbulence.

For the dwarf galaxies studied here, we evaluate Equation (2) using scale heights and velocity dispersions from the average values for 20 dIrrs in Elmegreen & Hunter (2015), in Table 2 of that paper. For the concentrations of pixel values corresponding to the outer regions of the galaxies, we take the average scale height and $v_{disp}$ at 2 scale lengths, which are $H = 850$ pc and $v_{disp} = 9.7$ km s$^{-1}$. For the inner regions, we take the values at 1 scale length, which are 540 pc and
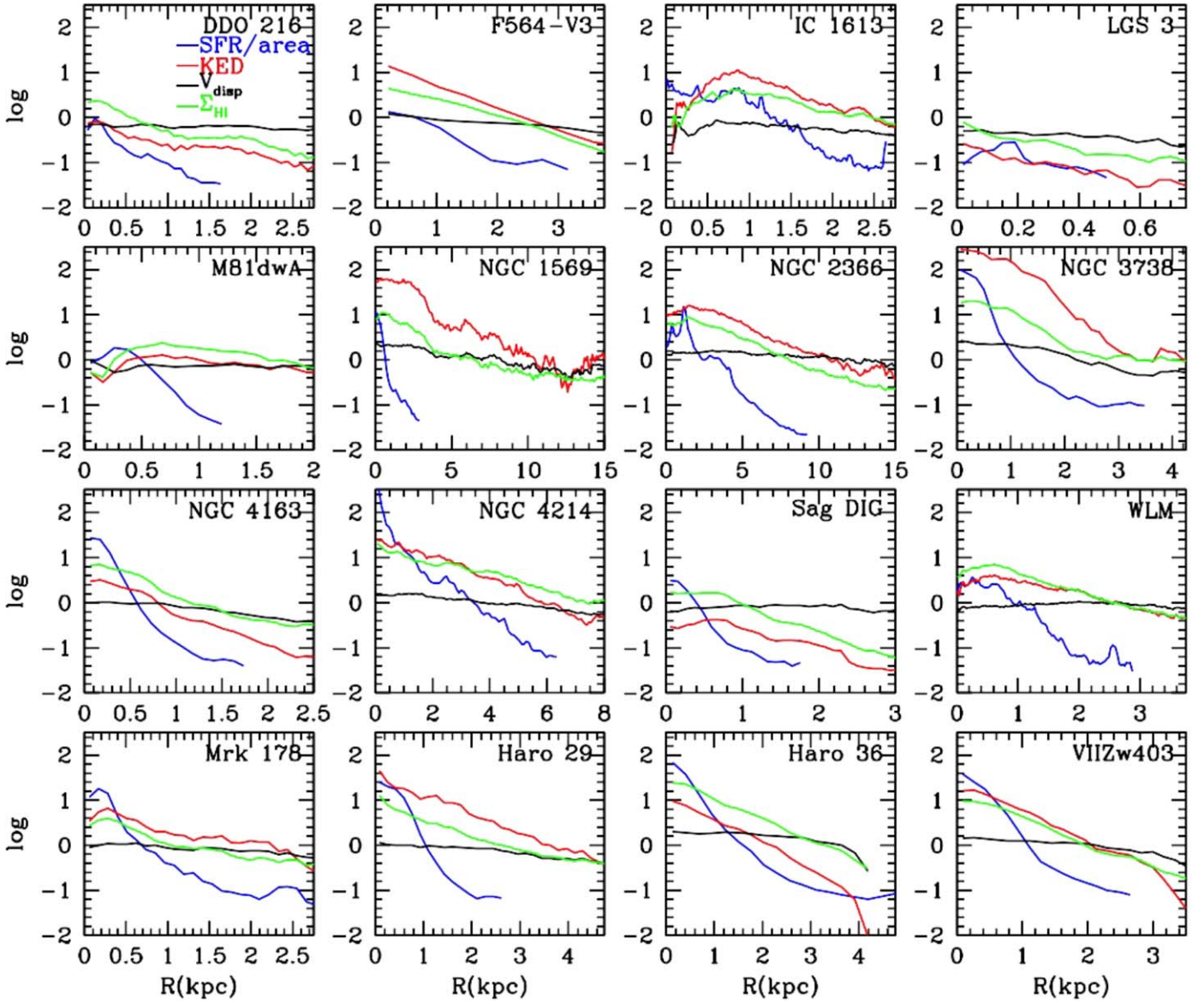
**Figure 10.** (Continued.)

$10.7\,\mathrm{km\,s^{-1}}$. We also include helium and heavy elements in the KED by multiplying the H I mass surface density by 1.36. Then, with $f_{cc}$ and $E_{SN}$ given above, Equation (2) is fitted for the efficiency in the two cases, using for the moment $v_{disp}$ instead of $v_{turb}$. The results are drawn as curves in the left panel of Figure 14. The average local efficiencies for the conversion of supernova energy to KED are $\eta = 0.0080 \pm 0.045$ and $0.0050 \pm 0.0075$ for the outer- and inner-disk regions, with these assumptions.

The total dispersions used to evaluate $\eta$ include thermal and turbulent motions, which were distinguished in several limiting cases by Bacchini et al. (2020) to get the desired $v_{turb}$. If we assume Mach $\sim 1$ turbulence in the general H I ISM, then $v_{turb} = v_{disp}/2^{0.5}$ and the derived values of $\eta$ decrease by a factor of 0.7, preserving the ratio $\eta/v$ used to match the KED. Alternatively, we could use thermal dispersions of $4.9\,\mathrm{km\,s^{-1}}$ and $6.1\,\mathrm{km\,s^{-1}}$ modeled for NGC 4736 and NGC 2403, respectively, by Bacchini et al. (2020) to estimate that $v_{turb}/v_{disp} \sim 0.8$, given that $v_{disp} \sim 10\,\mathrm{km\,s^{-1}}$ here. Then, our derived $\eta$ should decrease by $\sim 0.8$. The Bacchini et al. (2020)

galaxies were more massive than our dIrr galaxies, but the thermal contributions to $v_{disp}$ are not likely to be much different. These corrections change the average value of $\eta = 0.0065$ for the two regions in Figure 14 to $\eta \sim 0.0048$, using a mean correction factor of 0.75.

This $\eta$ value is the average for the peak regions of star formation. It measures how efficiently star formation energy gets into H I turbulent motions locally in units of the supernova energy per unit mass of young stars. When normalized this way, other types of energy related to star formation such as expanding H II regions and stellar winds are included in $\eta$, too. What is not included as a source of turbulent motion is energy unrelated to star formation, such as gravitational energy from gas collapse on the scale of the ISM Jeans length, or collapse energy from transient spiral arms driven by combined gas and stellar masses, or shock energy from the relative motions of gas and stellar spiral density waves. If $\eta \sim 0.0048$ measured locally gives the actual efficiency for star formation to pump turbulence in the H I gas, then the global turbulent energy pumped by all of the star formation in a galaxy should equal
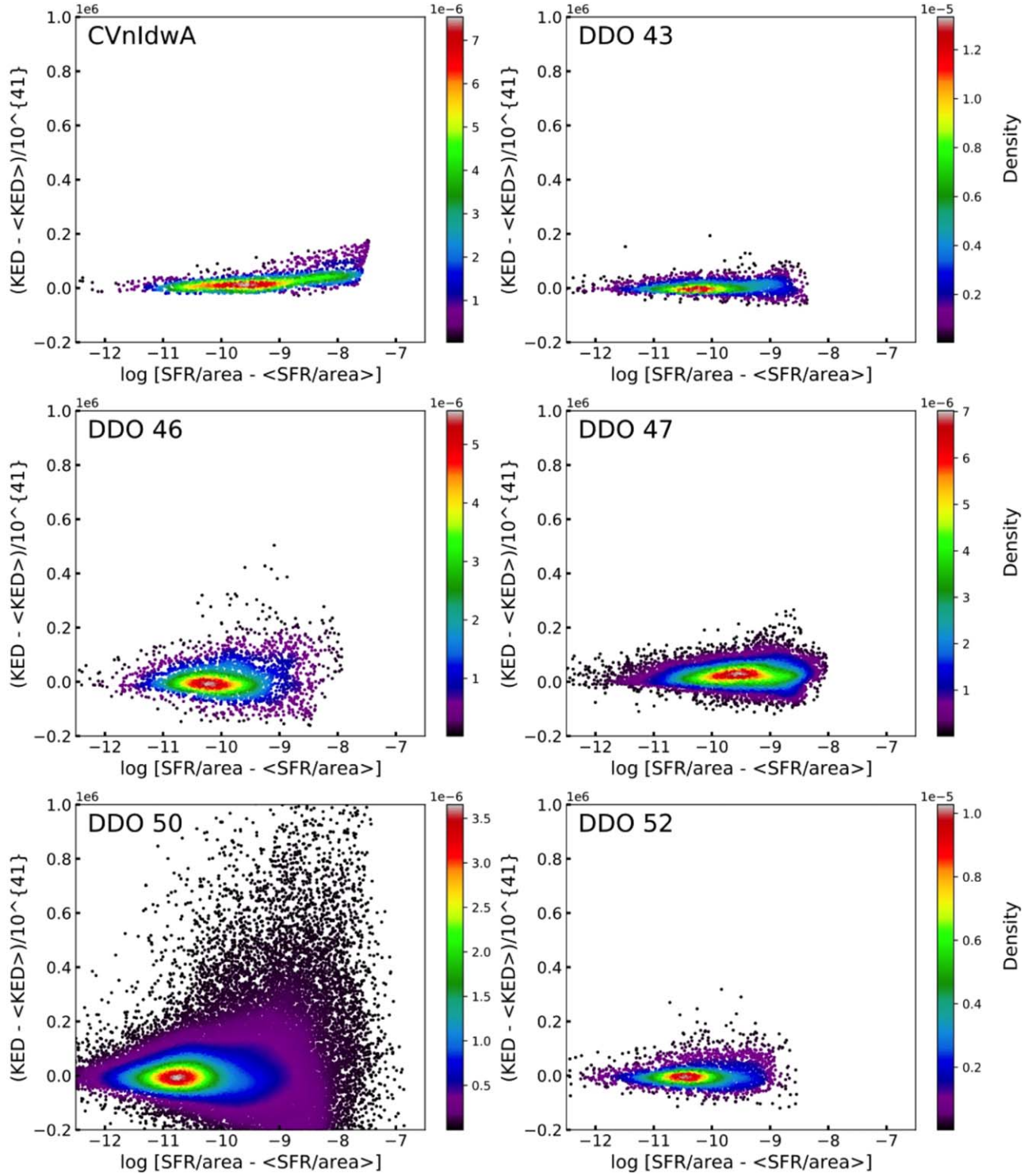
**Figure 11.** Pixel–pixel plots of the excess KED above the average value at each radius vs. the log of the excess $\Sigma_{\mathrm{SFR}}$. The density of points is color-coded. Figures for the rest of the galaxies in this study are available in the online materials. (There are 6 figures like this for 36 galaxies. The KED has not been corrected for He and heavy elements.). (An extended version of this figure is available.)

our local $\eta$ multiplied by the global SFR (along with the other factors in Equation (2)). Because Bacchini et al. (2020) found that the global turbulent energy is $1.5^{1.8}_{0.8}\%$ of the energy derived from the SFR, there would seem to be more energy required than what star formation alone can provide. The excess energy needed is a factor of $\sim 0.015/0.0048 - 1 \sim 2$ times the star formation energy.

This factor has many uncertainties, both from the range in global values derived by Bacchini et al. (2020) and from the galaxy-to-galaxy or inner-disk to outer-disk variations derived here. For example, our $\eta \sim 0.0048$ is closer to that of the dwarf galaxy DDO 154 in Bacchini et al. (2020), which had $\eta = 0.009$ assuming a pure warm phase H I. Also, our average $\eta$ for the inner-disk regions in Figure 14 was higher than the
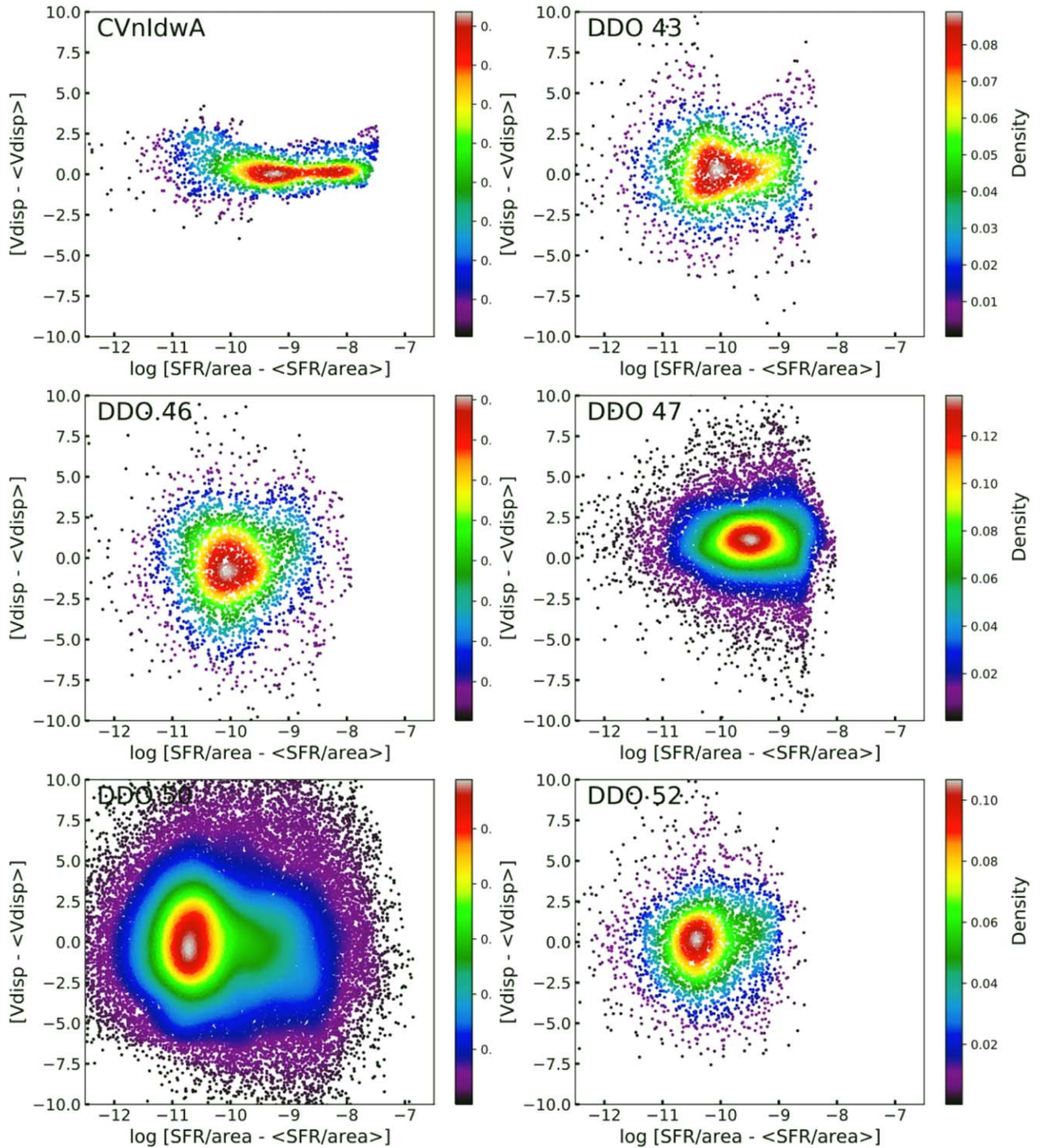
**Figure 12.** Pixel–pixel plots of the excess $v_{disp}$ above the average value at each radius vs. the log of the excess $\Sigma_{SFR}$. The density of points is color-coded. Figures for the rest of the galaxies in this study are available in the online materials. (The remaining 36 galaxies are shown in 6 figures). (An extended version of this figure is available.)

average for the inner and outer disks combined (which gave the value 0.0048) by a factor of 1.2. But even within this range, the global energy from turbulence seems to be larger than what can be pumped from star formation alone, if we use local SFRs as the basic means of calibrating $\eta$.

Figure 14 for the KED excess has two high points for the inner disk which were not included in the efficiency fit. These are the galaxies Haro 29 with excess KED $= 16 \times 10^{45}$ erg pc$^{-2}$ and NGC 1569 with excess KED $= 141 \times 10^{45}$ erg pc$^{-2}$.

Correspondingly, Figure 11 shows a scatter of individual pixel points to very high values of KED for these galaxies.

The middle panel of Figure 14 shows the average $v_{disp}$ excess at each concentration of excess $\Sigma_{SFR}$ in Figure 12. The excess velocity dispersion is rarely larger than 1 km s$^{-1}$ and averages 0.45 km s$^{-1}$ in the outer disk, $-0.34$ km s$^{-1}$ in the inner disk, and 0.37 km s$^{-1}$ overall. Some local star formation regions have lower H I velocity dispersions than the average at that galactocentric radius, giving negative excesses in Figure 14.
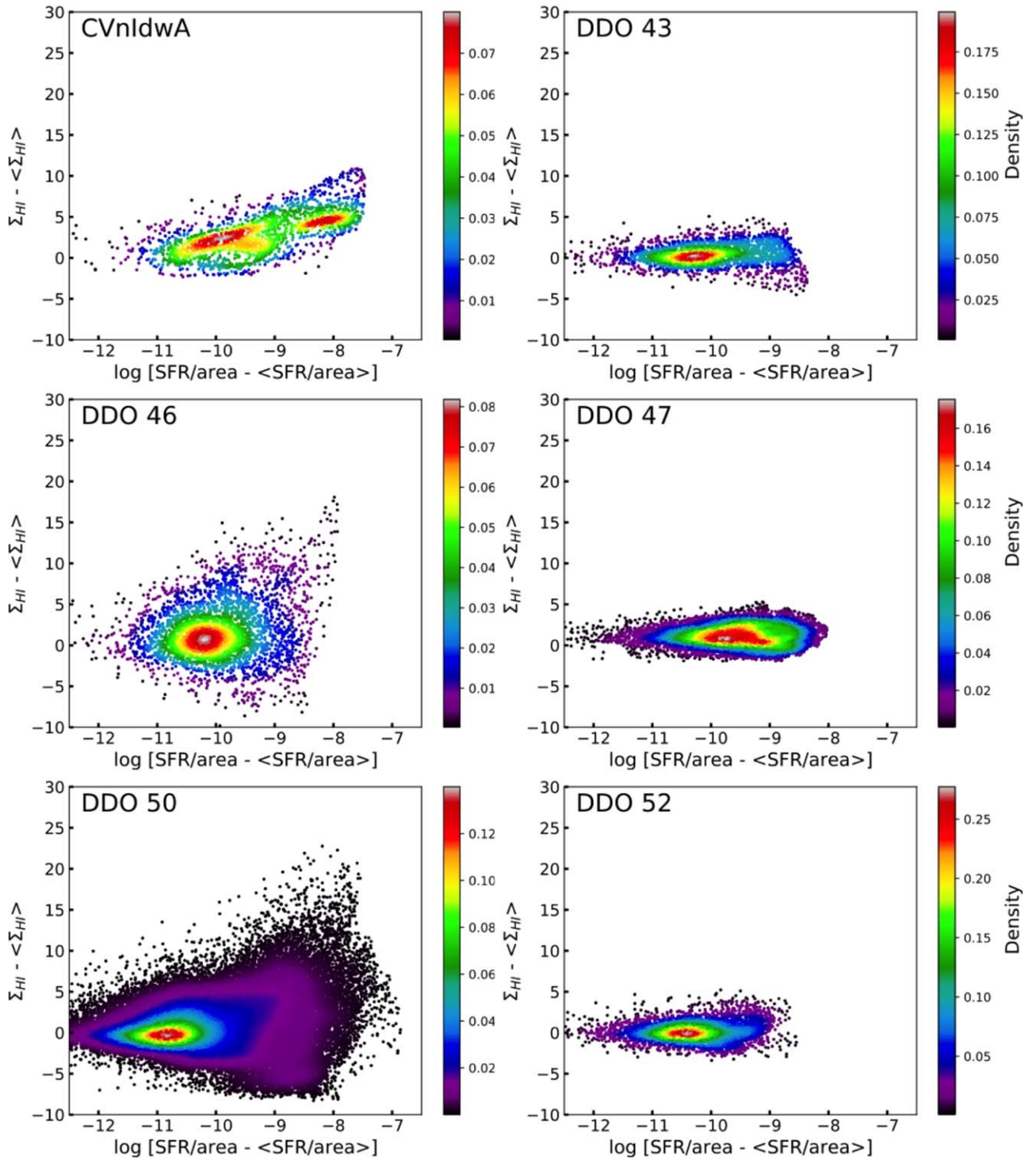
**Figure 13.** Pixel–pixel plots of the excess $\Sigma_{HI}$ above the average value at each radius vs. the log of the excess $\Sigma_{SFR}$. The density of points is color-coded. Figures for the rest of the galaxies in this study are available in the online materials. (The remaining 36 galaxies are shown in 6 figures). (An extended version of this figure is available.)

These typically small excesses in the local H I velocity dispersion are consistent with the small feedback efficiencies found above. There is relatively little generation of turbulence at the positions of star-forming regions.

The right-hand panel of Figure 14 shows the average $\Sigma_{HI}$ excess at each concentration of excess $\Sigma_{SFR}$ in Figure 13. There is a clear trend toward excess H I at local star formation regions, although in a few cases the H I is less than the

azimuthal average. This general excess corresponds to a ratio of $\Sigma_{HI}$ to $\Sigma_{SFR}$ that equals 6.5 Gyr in the outer disk, 1.2 Gyr in the inner disk and 1.6 Gyr overall, where this latter fit is shown by the curve in the figure. For this fit, the high point that is plotted in Figure 14 is excluded, that is, for NGC 1569, where the ratio is 31 Gyr. This average ratio of ∼1.6 Gyr is comparable to the consumption time for molecules, which is about 2 Gyr in Bigiel et al. (2008) and Leroy et al. (2008). If only molecular clouds
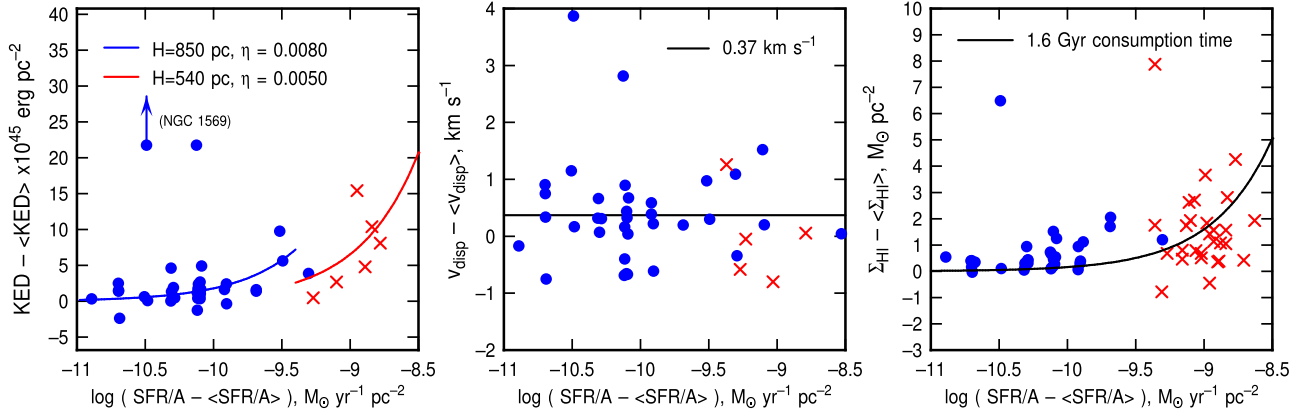
**Figure 14.** Mean excess KED corrected for He and heavy elements, $v_{disp}$, and $\Sigma_{HI}$ vs. the mean of the log of the (positive) excess $\Sigma_{SFR}$ for all galaxies. Dots correspond to the low-$\Sigma_{SFR}$ concentrations in the outer disks and crosses correspond to high $\Sigma_{SFR}$ in the inner disks. Left: the curves show the fitted relationships between the KED generated by supernovae and the $\Sigma_{SFR}$ for the indicated efficiencies of converting supernova energy into turbulence, and for galaxy scale heights of 850 pc and 540 pc. Middle: average $v_{disp}$ excess at each concentration of excess $\Sigma_{SFR}$ in Figure 12. The excess velocity dispersion averages 0.34 km s$^{-1}$ in the outer disk and 0.17 km s$^{-1}$ in the inner disk. Right: average $\Sigma_{HI}$ excess at each concentration of excess $\Sigma_{SFR}$ in Figure 13. There is a clear trend toward excess H I at local star formation regions.

form stars, then this similarity implies that the molecular fraction is about 50% in the inner disk, as suggested using other properties of H I and star formation in recent papers (Hunter et al. 2019, 2021; Madden et al. 2020).

## 5. Discussion

Comparisons between the KED or velocity dispersion and the local SFR using cross-correlations of several types and pixel-level excesses above the radial average quantities have shown virtually no connections between large-scale turbulence and star formation. Many of the galaxies have lumpy KED and FUV images but the lumps are not well correlated or anticorrelated spatially. This is contrary to some theoretical expectations and the simulations that have been designed to illustrate those expectations which suggest that feedback from star formation pumps a significant amount of interstellar turbulence, and thereby controls the interstellar scale height and average midplane density. While it is generally accepted that this midplane density controls the collapse rate of the ISM and therefore the average SFR, the origin of the turbulence and other vertical forces that determine the scale height and density have been difficult to observe directly. Most likely, the maintenance of a modest value for gravitational stability parameter $Q$ controls the overall interstellar turbulent speed through pervasive and mild gravitational instabilities, which also feed the star formation process through cloud formation. This was demonstrated by Bournaud et al. (2010) and also underlies the Feedback in Realistic Environments simulations by Hopkins et al. (2014); the primary role of feedback is to destroy molecular clouds locally (Benincasa et al. 2020). Our data suggest that this feedback does not extend far enough from molecular clouds to be visible in the H I at our resolution (from 26 pc at IC 1613 to 340 pc at DDO 52).

## 6. Summary

We have examined the relationship between star formation, as traced by FUV images, and turbulence in the gas, as traced by KED images and velocity dispersion maps in the LITTLE THINGS sample of nearby dIrr galaxies. We performed 2D cross-correlations between FUV and KED images, finding

maximum $C_{coef}$ that indicates little correlation. A plot of integrated SFR against the maximum $C_{coef}$ also shows no correlation. We also performed cross-correlations in annuli centered on the optical center of the galaxy to produce $C_{coef}$ as a function of radius. In some galaxies, the centers have $C_{coef}$ that are high enough to indicate a correlation, and in some galaxies, the $C_{coef}$ drops off with radius from the center.

To look at the images a different way, we determined the fraction of pixels in the FUV and KED images with values above a given percentage of the maximum pixel value in the image. Plots of these quantities show different behaviors for FUV and KED images in many of the galaxies. Finally, we considered on a pixel-by-pixel basis the excess KED, $v_{disp}$, and $\Sigma_{HI}$ above the average radial profiles of these quantities and plotted those versus the excess $\Sigma_{SFR}$. There was a weak tendency to have a higher excess KED at a higher excess $\Sigma_{SFR}$, corresponding to an efficiency of kinetic energy input to the local ISM from supernova related to star formation of about 0.5%. This is too small by a factor of about 2 for star formation to be the only source of global KED. The excess $v_{disp}$ connected with star formation peaks is also small, only 0.37 km s$^{-1}$ on average. The angular scale for these small excesses is typically 1″5, which, for a distance of 3 Mpc, corresponds to ~20 pc.

### ORCID iDs

Deidre A. Hunter https://orcid.org/0000-0002-3322-9798
Bruce G. Elmegreen https://orcid.org/0000-0002-1723-6330
Caroline E. Simpson https://orcid.org/0000-0003-3015-7300
Phil Cigan https://orcid.org/0000-0002-8736-2463

# References

Bacchini, C., Fraternali, F., Iorio, G., et al. 2020, A&A, 641, A70
Benincasa, S. M., Loebman, S. R., Wetzel, A., et al. 2020, MNRAS, 497, 3993
Bigiel, F., Leroy, A., Walter, F., et al. 2008, AJ, 136, 2846
Bigiel, F., Leroy, A., Walter, F., et al. 2010, AJ, 140, 1194
Bournaud, F., Elmegreen, B. G., Teyssier, R., Block, D. L., & Puerari, I. 2010, MNRAS, 409, 1088
Burkhart, B., Stanimirović, S., Lazarian, A., & Kowal, G. 2010, ApJ, 708, 1204
Chevance, M., Diederik Kruijssen,, J. M., & Krumholz, M. R. 2020, arXiv:2010.13788
Combes, F., Boquien, M., Kramer, C., et al. 2012, A&A, 539, A67
Deharveng, L., Zavagno, A., Anderson, L. D., et al. 2012, A&A, 546, A74
Dib, S., & Burkert, A. 2005, ApJ, 630, 238
Efremov, Y. N., & Elmegreen, B. G. 1998, MNRAS, 299, 588
Egorov, O. V., Lozinskaya, T. A., Moiseev, A. V., & Shchekinov, Y. A. 2017, MNRAS, 464, 1833
Elmegreen, B. G. 1993, ApJL, 419, L29
Elmegreen, B. G., & Efremov, Y. N. 1997, ApJ, 480, 235
Elmegreen, B. G., & Hunter, D. A. 2006, ApJ, 636, 712
Elmegreen, B. G., & Hunter, D. A. 2015, ApJ, 805, 145
Goldbaum, N. J., Krumholz, M. R., & Forbes, J. C. 2016, ApJ, 827, 28
Herrmann, K. A., Hunter, D. A., & Elmegreen, B. G. 2013, AJ, 146, 104
Hopkins, P. F., Kereš, D., Oñorbe, J., et al. 2014, MNRAS, 445, 581
Hopkins, P. F., Quataert, E., & Murray, N. 2011, MNRAS, 417, 950
Hunter, D. A., & Elmegreen, B. G. 2004, AJ, 128, 2170
Hunter, D. A., Elmegreen, B. G., & Berger, C. L. 2019, AJ, 157, 241
Hunter, D. A., Elmegreen, B. G., Dupuy, T. J., & Mortonson, M. 2003, AJ, 126, 1836
Hunter, D. A., Elmegreen, B. G., & Gehret, E. 2016, AJ, 151, 136
Hunter, D. A., Elmegreen, B. G., Goldberger, E., et al. 2021, AJ, 161, 71
Hunter, D. A., Elmegreen, B. G., & Ludka, B. C. 2010, AJ, 139, 447
Hunter, D. A., Elmegreen, B. G., Oh, S.-H., et al. 2011, AJ, 142, 121
Hunter, D. A., Elmegreen, B. G., Rubin, V. C., & Ashburn, A. 2013, AJ, 146, 92
Hunter, D. A., Elmegreen, B. G., & van Woerden, H. 2001, ApJ, 556, 773
Hunter, D. A., Ficut-Vicas, D., Ashley, T., et al. 2012, AJ, 144, 134
Hunter, D. A., & Plummer, J. D. 1996, ApJ, 462, 732
Ibáñez-Mejía, J. C., Mac Low, M.-M., Klessen, R. S., & Baczynski, C. 2017, ApJ, 850, 62
Joung, M. R., Mac Low, M.-M., & Bryan, G. L. 2009, ApJ, 704, 137
Kennicutt, R. C., Jr. 1989, ApJ, 344, 685
Kim, C.-G., & Ostriker, E. C. 2015, ApJ, 815, 67
Kim, J.-G., Kim, W.-T., & Ostriker, E. C. 2018, ApJ, 859, 68
Kingsburgh, R. L., & McCall, M. L. 1998, AJ, 116, 2246
Kraljic, K., Renaud, F., Bournaud, F., et al. 2014, ApJ, 784, 112
Krumholz, M. R., Burkhart, B., Forbes, J. C., & Crocker, R. M. 2018, MNRAS, 477, 2716
Krumholz, M. R., & McKee, C. F. 2005, ApJ, 630, 250
Lehnert, M. D., Le Tiran, L., Nesvadba, N. P. H., et al. 2013, A&A, 555, A72
Leroy, A. K., Walter, F., Brinks, E., et al. 2008, AJ, 136, 2782
Mac Low, M.-M., Burkert, A., & Ibáñez-Mejía, J. C. 2017, ApJL, 847, L10
Mac Low, M.-M., & Klessen, R. S. 2004, RvMPh, 76, 125
Madden, S. C., Cormier, D., Hony, S., et al. 2020, A&A, 643, A141
Maier, E., Chien, L.-H., & Hunter, D. A. 2016, AJ, 152, 134
Maier, E., Elmegreen, B. G., Hunter, D. A., et al. 2017, AJ, 153, 163
Martin, D. C., Fanson, J., Schiminovich, D., et al. 2005, ApJL, 619, L1
Meurer, G. R., Carignan, C., Beaulieu, S. F., & Freeman, K. C. 1996, AJ, 111, 1551
Ossenkopf, V., Krips, M., & Stutzki, J. 2008, A&A, 485, 917
Ostriker, E. C., McKee, C. F., & Leroy, A. K. 2010, ApJ, 721, 975
Padoan, P., Pan, L., Haugbolle, T., & Nordlund, Å. 2016, ApJ, 822, 11
Palmeirim, P., Zavagno, A., Elia, D., et al. 2017, A&A, 605, A35
Piontek, R. A., & Ostriker, E. C. 2005, ApJ, 629, 849
Stilp, A. M., Dalcanton, J. J., Skillman, E., et al. 2013, ApJ, 733, 88
Struck, C., & Smith, D. C. 1999, ApJ, 527, 673
Tamburro, D., Rix, H.-W., Leroy, A. K., et al. 2009, AJ, 137, 4424
Toomre, A. 1964, ApJ, 139, 1217
Übler, H., Genzel, R., Wisnioski, E., et al. 2019, ApJ, 880, 48
van Zee, L., Haynes, M. P., Salzer, J. J., & Broeils, A. H. 1997, AJ, 113, 1618
Varidel, M. R., Croom, S. M., Lewis, G. F., et al. 2020, MNRAS, 495, 2265
Walter, F., Brinks, E., de Blok, W. J. G., et al. 2008, AJ, 136, 2563
Willett, K. W., Elmegreen, B. G., & Hunter, D. A. 2005, AJ, 129, 2186
Youngblood, A. J., & Hunter, D. A. 1999, ApJ, 519, 55
Zhang, H.-X., Hunter, D. A., & Elmegreen, B. G. 2012, ApJ, 754, 29
Zhou, L., Federrath, C., Yuan, T., et al. 2017, MNRAS, 470, 4573